Lifetime Model Development for Super-critical CO2 CSP Systems

Bruce Pint
Rishi Pillai

May 2019

OAK RIDGE NATIONAL LABORATORY
MANAGED BY UT-BATTELLE FOR THE US DEPARTMENT OF ENERGY

Corrosion Science & Technology
Physical Sciences Directorate

Lifetime Model Development for Supercritical CO2 CSP Systems

Bruce Pint
Rishi Pillai

Final Technical Report (FTR)

a.	**Federal Agency**	Department of Energy	
b.	**Award Number**	DE-EE0001556	
c.	**Project Title**	Lifetime Model Development for Supercritical CO$_2$ CSP Systems	
d.	**Principal Investigator**	Bruce A. Pint Distinguished Research Staff Email: pintba@ornl.gov Phone: 865-576-289	
e.	**Business Contact**	Dominic F. Lee Program Manager Email: leedf@ornl.gov Phone: 865-241-0775	
f.	**Submission Date**	February 15, 2019	
g.	**DUNS Number**	099114287	
h.	**Recipient Organization**	Oak Ridge National Laboratory	
i.	**Project Period**	**Start:** 10/1/2015	**End:** 12/31/2018
j.	**Submitting Official Signature**		

Lifetime Model Development for Supercritical CO$_2$ CSP Systems

Executive Summary

A project to develop an industry-supported lifetime model for concentrating solar power (CSP) systems using supercritical carbon dioxide (sCO$_2$) as a working fluid in a >50% efficiency power block was conducted at Oak Ridge National Laboratory and Brayton Energy, LLC. Four commercial alloys, Haynes 282, Inconel 740H, alloy 625 and Fe-base Sanicro 25, were selected for evaluation based on industry feedback including three partner alloy manufacturers. The compatibility evaluations focused on two conditions: 300 bar industrial grade (IG) sCO$_2$ using 500-h cycles and 1 bar sCO$_2$ using 10-h cycles to simulate the solar duty cycle. The last two years of the project focused on completing long-term exposures (10-15 kh) at 750°C. In addition, companion experiments were conducted in 1 bar IG CO$_2$ using 500-h cycles and in non-CO$_2$ environments (air and O$_2$) to better understand the effects of pressure and CO$_2$. To understand the effect of sCO$_2$ on mechanical properties, creep and creep-fatigue rupture testing in sCO$_2$ and pressurized air was conducted on alloy tubes at 750°C. In creep, no sCO$_2$ debit was noted for the four alloys. In creep-fatigue, alloy 740H specimens showed a >2X debit in lifetime in sCO$_2$ compared to pressurized air with an 8 min cycle.

After more than 1,250,000 h of cumulative testing and over 200 metallographic evaluations of time series of specimens in each of the environments, it is clear that the Ni-based alloys are compatible with the sCO$_2$ environment and environmental degradation should not prevent a 30 year lifetime, including daily thermal cycling, for a sCO$_2$ CSP system. As proposed, there were thermodynamic and experimental indications that the sCO$_2$ environment may be detrimental to alloy performance. However, except for Fe-based alloy 25 specimens exposed in cyclic oxidation, there was no significant acceleration of reaction kinetics in sCO$_2$ compared to similar exposures in ambient air or O$_2$. Depth profiles by glow discharge optical emission spectroscopy (GDOES) have not shown any significant C uptake in any of the alloy surfaces and analytical transmission electron microscopy has noted changes in the oxide scale microstructure in sCO$_2$ and CO$_2$ compared to air oxidation but also not observed evidence of C ingress. The lack of C ingress and oxide scale spallation in these experiments required a change in strategy for the lifetime modeling with more emphasis on reaction products and Cr depletion.

The project benefited from a collaboration with a DOE Fossil Energy (FE) project which allowed comparisons with similar evaluations in research grade (RG) CO$_2$ (FE) at 750°C and 300 bar. The study of sCO$_2$ impurities suggested that impurities of 50 ppm O$_2$ and H$_2$O have minimal effect on the oxidation rate or reaction products at 750°C/300 bar. Regular conference calls and surveys with sCO$_2$ industry stakeholders have provided valuable feedback and numerous presentations and publications from this work have informed the community about the conclusions of this research project. Future work should partner with the STEP (Supercritical Transformational Electricity Production) facility to evaluate the effects of flowing sCO$_2$ under prototypical conditions and evaluate Fe-based alloys at lower temperatures to enable the use of less expensive alloys where appropriate.

Table of Contents

Background

There is considerable interest in the use of supercritical CO$_2$ (sCO$_2$) for power generation applications including nuclear, fossil and concentrated solar power (CSP) [Dostal 2006, Zhang 2006, Chacartegui 2011]. The use of a sCO$_2$ Brayton cycle operating at temperatures greater than 700°C has the potential to create efficiencies greater than 50% [Feher 1968]. Initial compatibility work above 700°C in sCO$_2$ has shown relatively low reaction rates for relevant Ni-base structural alloys [Oh 2006, Olivares 2015, Pint 2015a, Pint 2016a, Pint 2017a]. A significant concern is the possible internal carburization that primarily has been seen for Fe-base alloys in 1 bar CO$_2$ [McCoy 1965, Meier 2010, Gheno 2011, Gheno 2013, Young 2014, Nguyen 2015]. As pointed out by several authors over the past 50 years [e.g. Fujii 1967, Meier 1982, Young 2011], the real concern for sCO$_2$ and other C-containing gases is not the carbon activity in the gas but the carbon activity at the metal-scale interface. A unique aspect of the CSP application is the daily thermal cycling, which previously has been briefly studied for CSP Air-Brayton cycles [Pint 2011, Pint 2013]. The current project has a goal of studying the long-term behavior of four alloys (Inconel 740, Haynes 282, Sanicro 25 and alloy 625) in CO$_2$/sCO$_2$ in order to develop a CSP-relevant lifetime model. In Year 1 of the project, 1000 h exposures were conducted at 1 and 300 bar at 700°-800°C and found low reaction rates. The 1 bar work was included in order to conduct 10-h thermal cycling, which is not possible in a 300 bar autoclave. Year 2 and Year 3 of the project focused on longer exposures at 750°C.

To put this work in context, a number of groups are actively involved in supercritical CO$_2$ (sCO$_2$) compatibility research and Figure 1 attempts to capture the temperature and pressure conditions that have been evaluated to date [Oh 2006, Dunlevy 2009, Furukawa 2010, Furukawa 2011, Tan 2011, Rouillard 2011, Cao 2012, Firouzdor 2013, He 2014, Saari 2014, Pint 2014, Lee 2014, 2015, Olivares 2015, Dheeradhada 2015, Pint 2015a, Mahaffey 2016, Kung 2016, Pint 2016a, Pint 2016b]. From Figure 1 it is clear that the ORNL experimental work at 300 bar and 700°-800°C in this project is evaluating the highest temperatures and pressures. Much of the previous long-term testing was conducted at 400°-650°C in support of nuclear energy applications particularly at JAEA [Furukawa 2011]. The JAEA work at 100 and 200 bar was the first to identify that sCO$_2$ pressure played a limit role in the corrosion rate at 400°-600°C. Recent work at ORNL sponsored by DOE FE found a similar result at 750°C (125-300 bar) [Pint 2016b, Pint 2017a]. Thus, only one sCO$_2$ pressure is being explored in this study.

Figure 2 shows a summary of some of the measured rate constants available in the literature along with the rate constant metric for this project. In general, conventional steels (Fe-Cr or Fe-Ni-Cr do not have sufficient oxidation resistance to meet the metric at 700°-800°C. In contrast, a number of Ni-base appear to have sufficient oxidation resistance up to 800°C. In Figure 2, the majority of data points above 700°C are from this study. The only other data points are from Wisconsin at 750°C [Dheeradhada 2015, Mahaffey 2016]

A 2015 paper reported sCO$_2$ exposures on pressurized tubes that were gun drilled from bar stock in some cases [Olivares 2015]. Internal carburization was observed on type
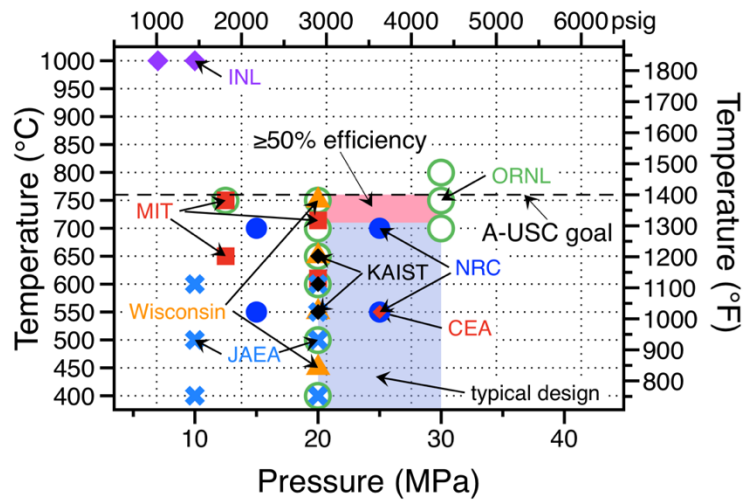
Figure 1. Published sCO$_2$ studies as a function of temperature and pressure [Pint, 2017b].

316 stainless steel after 550h at 650°C and 20MPa CO$_2$. The authors suggested that testing under stress is superior to exposure of coupons (without stress) but provided no data to substantiate this hypothesis. The results in this study were similar to results from Wisconsin [Cao 2012]. Tubes of Ni-based Hastelloy C276 formed a protective chromia scale for up to 1000h at 750°C in 20 MPa CO$_2$. These results are consistent with prior ORNL work on similar alloys. The reduced internal attack for C276 was attributed to the more protective chromia scale and lower C solubility in Ni-base alloys compared to steels.
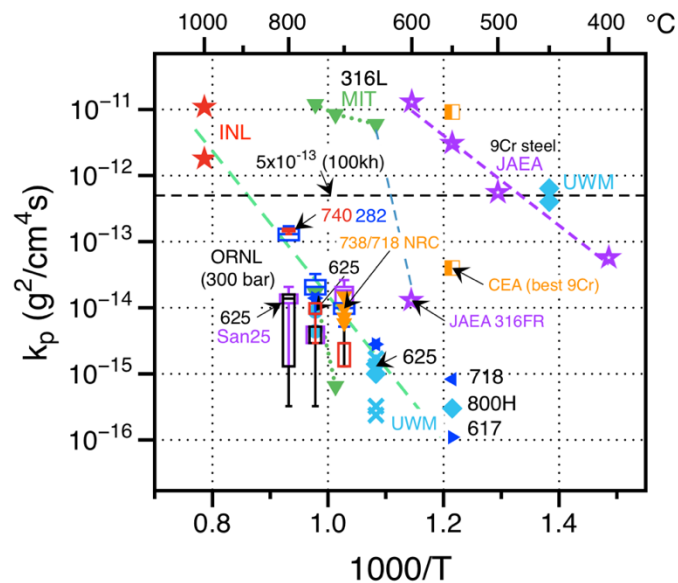
Figure 2. Published or calculated rate constants from data in the literature. Boxes show rate constants for 6-10 samples from this study [Pint, 2017b].

At the 5th International Symposium on Supercritical CO_2 Power Cycles held in San Antonio, TX in March 2016, there were several presentations on sCO_2 compatibility including two on impurity effects [Kung 2016, Mahaffey 2016]. Kung et al. found relatively little effect of high (1-5%) impurity levels of O_2 and H_2O to simulate an open "Allam" cycle for fossil energy [Allam 2013]. Mahaffey et al. compared the oxidation behavior of alloys 230 and 625 at 650° and 750°C in 20 MPa of research grade CO_2 and CO_2 with 100 ppm O_2. They found a substantial increase in the oxide thickness after 1000h at 750°C (5 x 200-h cycles) and some increase after a similar exposure at 650°C. The authors suggest that O_2 should be limited in the sCO_2 environment and are continuing to study this issue with O_2 additions of 7 ppm. The results are quite unusual and the authors did not appear to offer a mechanism for this observed detrimental effect of O_2. One conclusion is that the effects of impurities have not been entirely resolved.

Researchers at KAIST have studied a range of Fe- and Ni-base alloys at 550°-650°C in 200 bar sCO_2 for 1000 h [Lee 2014, 2015]. Since the 1000 h exposures were isothermal, no reaction rates were determined for Figure 2. However, the results were consistent with other studies with 9%Cr steel specimens showing the highest mass gains and the mass gain for 316-type steels increasing significantly between 550° and 650°C. The Ni-base alloys 600, 625 and 690 showed low mass gains at all temperatures. Similar to another study at 550°C [Dheeradhada 2015], transmission electron microscopy (TEM) of reaction products on 600, 690 and 800HT after exposure at 600°C also showed an amorphous, C-rich layer forming beneath crystalline Cr_2O_3 [Lee 2015]. However, only the Fe-base alloy 800HT showed internal carburization in the adjacent alloy, suggesting that Ni-base alloys are more resistant to internal carburization than Fe-base alloys. Figure 3 shows the greater amount of C uptake in the 800HT specimen at 600°C using secondary ion mass spectroscopy (SIMS) compared to the Ni-base alloys 600 and 690.

Finally, a 2017 paper [Gong 2017] represents an excellent initial model for the end of life for Grade 9 (Fe-9Cr-1Mo) steel fins in the British advanced gas-cooled reactors (AGRs). The model benefitted from extensive laboratory data generated by the
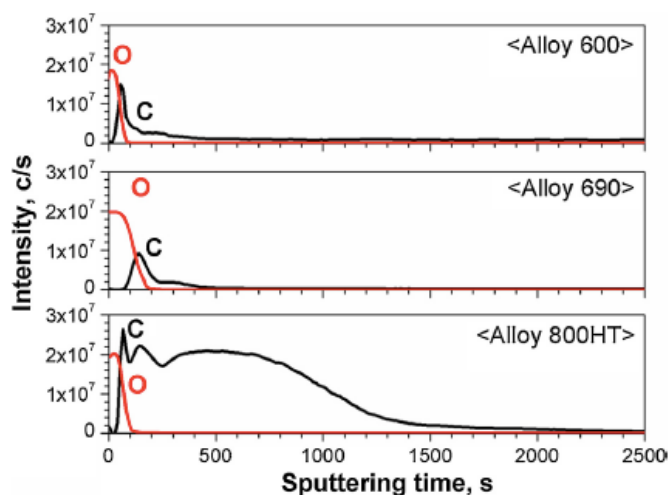

Figure 3. Secondary ion mass spectroscopy of alloys exposed for 1000 h at 600°C in 200 bar sCO_2 [Lee 2015].

operators (now EDF, based in France). The data set reported in the paper shows Grade 9 specimens exposed for up to 80,000 h in ~40 bar CO_2-1%CO at 580°-640°C, Figure 4a. (At the 10th Microscopy of Oxidation conference in the UK in April, one poster showed laboratory data for 180,000 h.) At the end of life, when the oxide growth rate accelerates (i.e. breakaway oxidation), all of the Cr in the steel is tied up in carbides representing ~25 vol.% after ~20,000 h at 600°C, Figure 4b. The model then predicts that for operation near 500°C, breakaway oxidation will not occur for ~200 years. One reason for the long life is that the mass gain (both O and C uptake) at breakaway appears to increase with decreasing temperature. This is an empirical observation without a clear explanation. There are several differences between sCO_2 and the AGR environment. First the AGR pressure is lower, only ~43 bar. Second, the AGR C activity is much higher (with much lower O partial pressure to prevent attack of the graphite moderators in the reactor core), ~0.1 vs. 10^{-13} for sCO_2 without impurities.

In summary,

1. Other groups are studying compatibility of similar alloys in sCO_2, but none are covering the temperatures and pressures being investigated at ORNL and few have used industrial grade CO_2.

2. Few groups have studied oxidation in 10-h cycles under any conditions and no other cyclic oxidation data have been identified in CO_2. ORNL has relatively unique experimental equipment to conduct these experiments.

3. Impurity (O_2, H_2O) effects in sCO_2 are being investigated but a consistent understanding of their role has not emerged. The current SunShot and Fossil Energy (FE) sCO_2 projects at ORNL will assist in addressing this issue.

4. During the project, ORNL's characterization began employing more sophisticated characterization techniques such as TEM and GDOES (Glow discharge optical electron spectroscopy) to assist in locating C ingress and studying the thin reaction products.
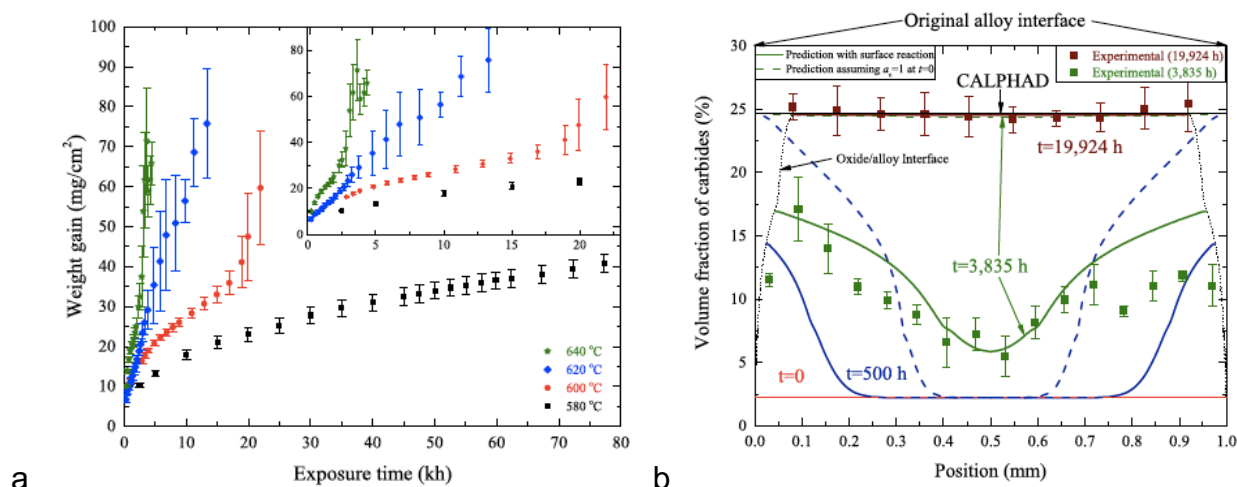

Figure 4. (a) archival mass gain data for Fe-9Cr-1Mo steels at 43bar in reducing CO_2 and (b) a model to fit measured carburization data of 9%Cr steel [Gong 2017].

Project Objectives

This three-year project sought to develop a lifetime model for materials in supercritical carbon dioxide (sCO_2) conditions relevant to concentrated solar power (CSP) applications. Experimental work will generate relevant corrosion, creep and fatigue data to populate the model and then verify the model predictions. The lifetime model will assist in enabling low-cost, high-efficiency commercial CSP systems operating at ≥720°C.

Year 1 tasks/subtasks were broken down per the following:

1.1 Industry interaction

1.2 Conduct testing in carbon dioxide environment

  1.2.1 300 bar experiments in sCO_2

  1.2.2 Creep rupture testing in sCO_2 and air

  1.2.3 1 bar experiments in 10-h cycles

1.3 Modeling and Characterization

  1.3.1 Thermodynamic calculations

  1.3.2 Carburization depth characterization

  1.3.3 Modeling

Phase 1 milestone

Year 2 tasks/subtasks were broken down per the following:

2.1 Conduct testing in carbon dioxide environment

  2.1.1 300 bar experiments in sCO_2 at 750°C

  2.1.2 Creep rupture testing in sCO_2 and air

  2.1.3 1 bar experiments in 10-h cycles

  2.1.4 300 bar experiments in sCO_2 at 700°C

2.2 Modeling and Characterization

  2.2.1 Carburization depth characterization

  2.2.2 Modeling

2.3 Industry interaction

Phase 2 milestone

Year 3 tasks/subtasks were broken down per the following:

3.1 Industry feedback to assess the project

3.2 Complete testing in carbon dioxide environment

  3.2.1 Complete 500-h cycle testing at 750°C in sCO_2

  3.2.2 Complete creep-fatigue testing at 750°C in sCO_2

3.2.3   Complete 10-h cycle testing at 750°C in CO_2

3.2.4   Conduct testing in controlled impurity sCO_2

3.3   Modeling and Characterization

3.3.1   Carburization depth characterization

3.3.2   Modeling

Project Results and Discussion:

This section is broken down by task.

Task 1.1 Industry Feedback

Subtask 1.1.1: Contact companies that design and manufacture sCO_2 CSP systems and alloy manufacturers.

The first objective for this project was to identify the four alloys to be studied. The three alloy-producing project partners each selected one of their alloys (Haynes 282, Special Metals 740H and Sandvik Sanicro 25). The fourth alloy was selected based on an industry survey conducted in October and early November. In total, 10 companies responded and their votes were tallied with a 1st choice given 3 points, 2nd choice 2 points, 3rd choice 1 point and 0.5 points for other alloys mentioned. (Complete results were provided in the Phase 1 report.) Alloy 625 was selected as the fourth alloy based on the highest point total and being mentioned on 6 surveys.

A second conference call was held in April 2016. The limited specific feedback obtained included considering adding additional alloys such as 230 and 617 to the study. While those alloys could not be accommodated in this project, alloys 230 and 617 were studied in the DOE FE project at ORNL [Pint 2014, 2015a, 2016a, 2016b, 2016c, 2016d, 2017a, 2018c,2019b]. Overall, the outcome of this task was very positive, ORNL established contact with a number of new industrial stakeholders and succeeded in educating the industry about the merits of PS Ni-base alloys 740 and 282.

Task 1.2 Conduct testing in carbon dioxide environment

With a special thanks to the project industrial partners, plate and tube (for creep testing) of all four alloys was received and the measured chemistries of the plate material are shown in Table 1. Coupons (~1.5x11x19mm or ~1.5x12x20mm) were machined of each material and were polished to a 600 grit finish and ultrasonically cleaned in acetone and methanol prior to testing. All of the experiments used industrial grade (IG) CO_2 (<50ppm O_2, 18.8±16.9 ppm H_2O, measured in 10 cylinders). Specimen mass change data was measured on a Mettler Toledo model XP205 with an accuracy of ~0.04mg or ~0.01mg/cm^2. More details of the experimental procedure are available [Pint 2014a, Brese 2017].

Subtask 1.2.1: Conduct 500-h cycle testing at 700°-800°C in sCO_2

For this subtask, six specimens of each alloy were exposed to 300 bar IG sCO_2 at 700° and 800°C and 11 of each at 750°C, as this temperature will be continued for longer

Table 1. Chemical composition of the four alloys that are being studied in this project in mass% measured by inductively coupled plasma and combustion analyses.

Alloy	Fe	Ni	Cr	Al	Co	Mo	Nb	Ti	Mn	Si	W	Other
25	42.6	25.4	22.3	0.03	1.5	0.2	0.5	0.02	0.5	0.2	3.5	3.0Cu,0.2N
282	0.2	57.1	19.6	1.6	10.6	8.6	<	2.2	0.02	0.04	0.01	
740H	0.1	49.7	24.5	1.4	20.6	0.3	1.5	1.4	0.3	0.2	<	
625	4.0	61.0	21.7	0.12	0.1	8.8	3.5	0.2	0.2	0.2	0.06	0.09Cu

Note: < is less than 0.002%

times in Phases 2 and 3. Mass change results are shown for 2 alloys in Figure 5a and the rate constants are plotted on an Arrhenius plot in Figure 5b. A 500-h exposure time was selected for these experiments based on prior work and the ~6-8 h needed to bring the autoclave to the desired temperature and pressure. However, this meant that only two data points were available to generate a rate constant. The rate constants were generated by plotting the specific mass change versus the square root of time [Pieraggi 1987]. Ideally, more than two data points would be used to generate a rate constant. For alloy 625 in Figure 5a, all of the mass gains were low and there was some scatter in the measurements. For alloy 740 (similar to 282), the mass gains were higher due to the internal oxidation of Al and Ti (Table 1) as well as the incorporation of Ti into the Cr_2O_3 scale, which appears to accelerate the oxide growth [Ennis 1985, Brady 2006, Pint 2015b]. As can be seen from Figure 5b, the rate constants for 282 were similar to 740 at 800°C, but more scatter was noted at the lower temperatures. This may be due to the higher Al and Ti contents in 282 affecting the rate at a lower temperature but this composition difference may be less critical at 800°C. Sanicro 25 represented an
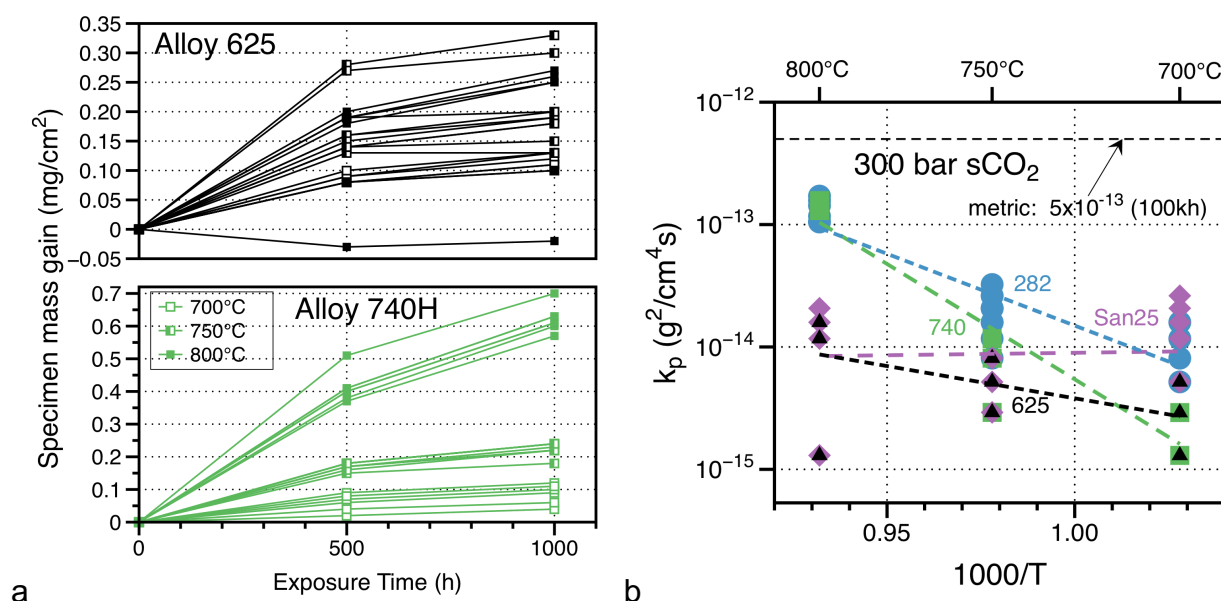

Figure 5. (a) alloy specimen mass change data for 2 alloys exposed for 500-h cycles in 300 bar IG sCO₂ at 700°-800°C, (b) Arrhenius plot of the rate constants measured.

unusual result that the rates at 700°C were higher than at 750° or 800°C. Subtask 1.2.3 found a similar result at 700°C after longer times.

The dashed lines in Figure 5b are an exponential (Arrhenius) fit to the data. All of the lines increase with temperature as expected except for Sanicro 25 due to the high values measured at 700°C. Based on the rate constants generated, all of the average rate constants were below the metric of 5 x 10^{-13} g^2/cm^4s, Figure 5b. Above 700°C, the alloys fall into two pairs. The PS Ni-base alloys, 740H and 282, have similar rates and Sanicro 25 and 625, without significant Ti and Al, both have lower rates.

As noted in the Background section, this is the first time that rate constants were measured at such a combination of high temperature and pressure. One uncertain aspect of these results is how the impurities in the IG CO_2 may have affected the rate constants. However, the DOE FE project exposed the same alloys for 5,000 h in research grade (RG) sCO2 (<5ppm O_2, 4.1±0.7 ppm H_2O, measured in 6 cylinders) and found similar mass gains [Pint 2018d, 2019b].

Subtask 1.2.2: Conduct creep rupture testing at 700°-800°C in sCO_2

This subtask was conducted at Brayton Energy, LLC (BE) in a rig previously constructed with DOE funding, Figure 6a. The control system was modified to accommodate creep rupture testing outlined in this subtask. Special Metals was first to provide tubing of 740H for testing and this alloy was selected for Phase 1 testing. Upon calculating the stresses needed for rupture, BE determined that the 740H wall thickness needed to be machined down to ~2.1mm to minimize the stress (i.e. gas pressure) needed in the experiments. Example specimens are shown in Figure 6b.

Figure 7 show the results of 22 rupture experiments. The ruptures varied from small defects to extensive deformation with examples shown in Figure 8. There were slight differences in the lifetimes measured in air and sCO_2 but the differences were not statistically significant. A conclusion from this task was that Phase 2 testing on the other alloys would focus on longer times and lower stresses.
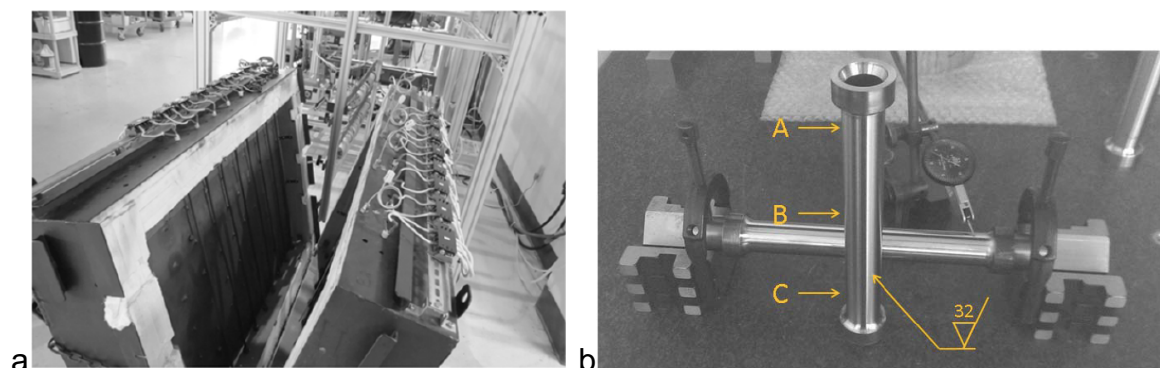

Figure 6. (a) The BE creep rig and (b) machined 740H creep specimens (right) that are 203mm long and had the wall thickness reduced to 2.1mm for these experiments.
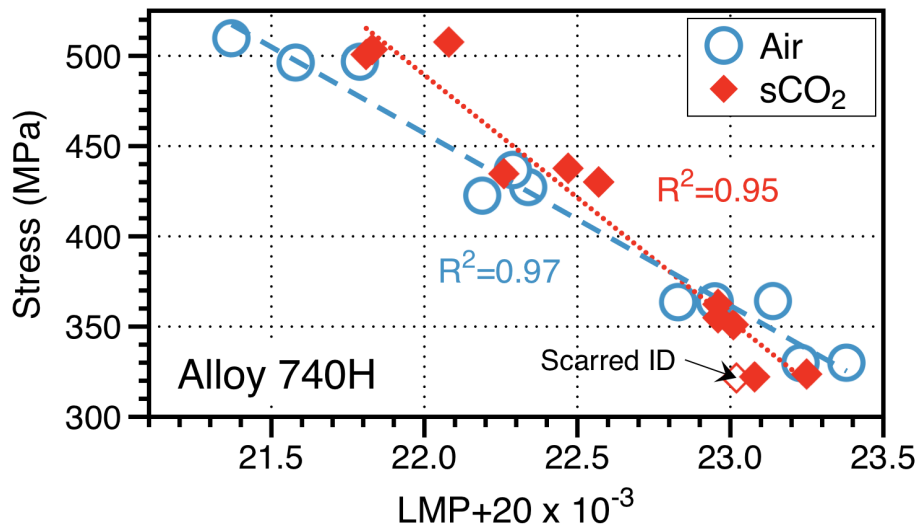
Figure 7. Larson Miller Parameter (LMP) calculated for each rupture versus the applied hoop stress is shown for the sCO$_2$ and pressurized air experiments.

Subtask 1.2.3: Conduct 10-h cycle testing at 700°-800°C in CO$_2$

Initial 1,000 h exposures (100 x 10-h cycles) were completed for two specimens of each alloy at three temperatures (700°, 750° and 800°C). Another set of three specimens of each alloy was exposed to 4000 h (400 x 10-h cycles) at 700° and 800°C. Automated cyclic rigs are run for one week intervals (16 cycles) with each cycle consisting of 10-h at temperature in 1 bar IG CO$_2$ (100 cc/min) followed by 10 min cooling out of the furnace in air to < 30°C. The specimens are weighed each week. Figure 9 summarizes the mass change data from 700° and 800°C. At 700°C, the mass gains were very small for 625 and 740H, <0.1mg/cm^2 total mass gains after 4,000 h exposures. For the 625 specimens, all of the specimens began to lose mass after ~1,500 h and no rate
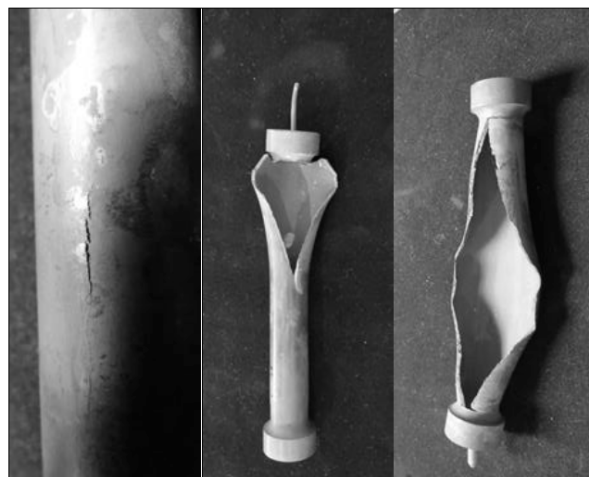

Figure 8. Various failure modes from small defects to extensive deformation.
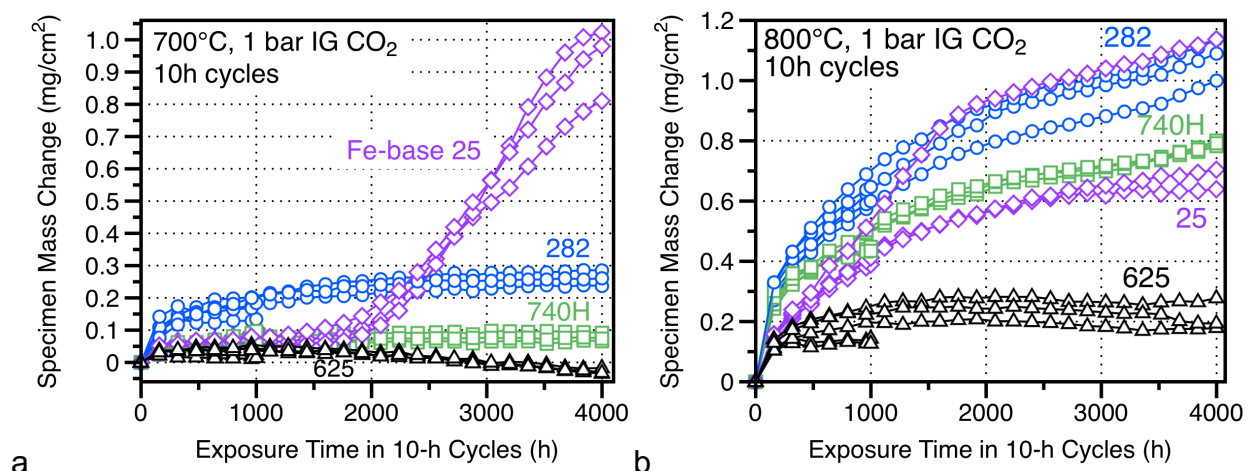
Figure 9. Specimen mass gain during 10-h cycles in 1 bar IG CO$_2$ at (a) 700°C and (b) 800°C. Two specimens of each alloy were stopped at 1000 h for characterization. The other three specimens were exposed to 4,000 h. [Pint 2017c, Pint 2018a]

constants could be measured. Linear mass losses [Tedmon 1966] were observed in other experiments and were attributed to Mo evaporation and not to scale spallation. Spallation in thermal cycling requires the strain energy in the oxide to exceed the interface adhesion [Evans 1995]. With these small mass gains, the oxides were presumably <1 µm thick and should not spall. The 282 specimens consistently gained mass at 700°C, showing the most regular behavior. Surprisingly, the three Sanicro 25 specimens exposed at 700°C exhibited a much higher mass gain after ~1500 h of relatively low mass gains and then gained mass at a much higher rate, Figure 9a. At 800°C, mostly parabolic behavior was observed, Figure 9b. One of the three Sanicro 25 specimens showed a higher mass gain than the other two specimens but has not shown an accelerated rate as at 700°C. The cyclic oxidation results at 750°C are summarized in section 3.2.3

The metric for this milestone was an evaluation of the rate constant, similar to section 1.2.1. The rates were calculated by plotting the mass change data versus the square root of time and using a linear fit of the slope [Pieraggi 1987]. For the Sanicro 25 specimens at 700°C, fits were made before and after the accelerated mass change. At 750°C, the rates were calculated after 1,000 h exposures from Phase 1. Figure 10 is an Arrhenius plot of the calculated rate constants. After the acceleration, the alloy 25 specimens no longer meet the 5 x 10^{-13} g^2/cm^{4}s metric shown by the dashed line in Figure 10. As mentioned above, rates could not be calculated at 700°C for alloy 625 and only one rate at 750°C because of small mass losses in the 625 specimens. This was not an issue in the 300 bar experiments, Figure 5b.

Task 1.3 Modeling and Characterization

This is a key task in terms of characterizing the reaction product and developing the lifetime model. The subtasks were basic in Phase 1 as data were being collected.
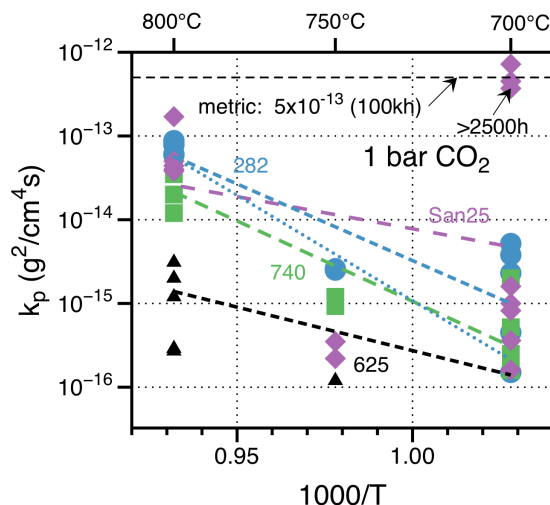
Figure 10. Arrhenius plot of the rate constants measured in 1 bar IG CO₂ using 10-h cycles.

Subtask 1.3.1: Conduct thermodynamic calculations about predicted reaction products in sCO₂ at 600°-800°C and 1-300 bar.

The goal of this subtask was to make an initial assessment of the thermodynamics of the sCO₂ environment in the temperature, pressure and impurity range of interest. Carburization can occur according to the following reaction:

$$2CO(g) = C(s) + CO_2(g) \qquad (1)$$

The carbon activity (a_C) in the gas phase can be calculated from the following equation:

$$\Delta G^{\circ}_1 = -RT \ln (a_C \cdot p_{CO_2}/p_{CO}^2) \qquad (2)$$

where ΔG°_1 is the Gibb's free energy for reaction 1 and p_{CO_2} and p_{CO} are the partial pressures of CO_2 and CO, respectively. In a pure CO_2 environment, p_{CO_2} can be approximated as the total pressure, and p_{CO} can be found with equation 3:

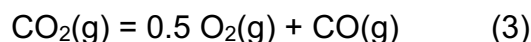$$CO_2(g) = 0.5\ O_2(g) + CO(g) \qquad (3)$$

Figure 11 shows the results of this calculation for the carbon activity as a function of temperature. The carbon activity is seen to have a strong dependence on temperature but the values are all quite low and not a cause for concern.

As pointed out by several authors over the past 50 years [e.g. Fujii 1967, Meier 1982, Young 2011], the real concern for sCO₂ and other C-containing gases is not the carbon activity in the gas but the carbon activity at the metal-scale interface. As the p_{O_2} drops in the scale from that in the gas to the metal-oxide equilibrium (e.g., the Cr/Cr₂O₃ equilibrium), Equation 3 indicates that p_{CO} will increase and, based on Equation 1, a_C will also increase. The amount of the a_C increase will depend on which oxide is being considered. For a total pressure of 1 atm, Figure 12 shows that the a_C values can be very high for the more stable oxides. For the less stable Fe₂O₃, the a_C values were lower but a_C values greater than 1 were observed for Cr₂O₃ and Fe₃O₄ below ~640°C.
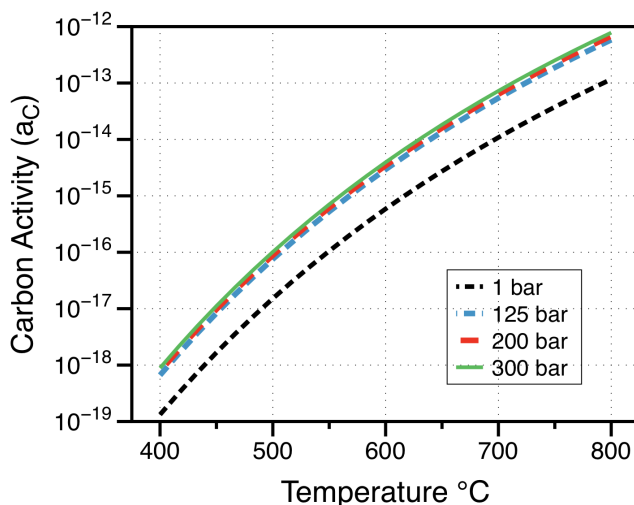
Figure 11. Activity of carbon versus temperature in a pure CO$_2$ environment

These high values suggest that internal carburization or metal dusting is possible and that is the primary concern for studying sCO$_2$ compatibility. Two caveats about Figure 12 are (1) the oxygen pressure is assumed to be fixed by the metal-oxide equilibrium, therefore the calculation is independent of the O content of the gas, and (2) the total pressure is assumed to be 1 atm. For a solid metal-scale interface, this gas pressure may be unrealistically high. However, the gas pressure at the metal-oxide interface is not known. If one assumes the total pressure is lower within the scale, the carbon activity would decrease proportionally.

Figure 12. Calculated carbon activity at the metal-scale interface as a function of temperature for various surface oxides.

The higher C solubility for Fe-base alloys (e.g., alloy 25) makes them more susceptible to this form of attack than Ni-base alloys with a lower C solubility [Olivares 2015]. This 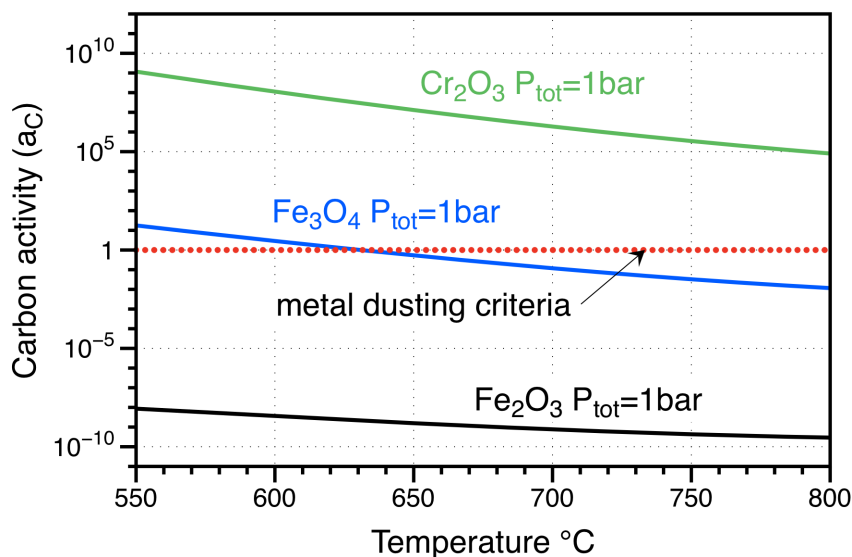may explain why alloy 25 showed higher mass gains at 700°C than the other alloys. Also, Figure 12 shows that a_C value is expected to decrease with increasing temperature. Again, this may explain why the accelerated attack was observed at 700°C but not at higher temperatures.

Subtask 1.3.2: Characterize specimens exposed to high and low pressure CO_2 to correlate mass change data with microstructural observations such as reaction product thickness and depth of metal affected.

This subtask involved the metallographic analysis of at least 48 samples (2 conditions x 3 temperatures x 4 alloys x 2 samples per condition). Figure 13 shows example images of the metallographic cross-sections produce that were imaged using light microscopy. The Cu-plating in Figure 14 worked well to easily identify the surface oxide. Based on other sCO₂ studies [e.g. Olivares 2015], etching the polished specimens with aqua regia to highlight any carburization or other microstructure features was evaluated. Figure 13 shows several examples where the alloy grain structure, grain boundary and internal precipitates, internal oxidation and γ' (Ni₃(Al,Ti) strengthening precipitates in 740 and 282) denuded zone were evident after etching on the right side. Example oxide thickness measurements in Figure 14 were made on unetched images and the internal oxidation measurements were made on etched images as in Figure 13. The oxide thickness measurements for two specimens were combined in one box, while the internal oxidation boxes were separated by specimen. In addition to the etching to look
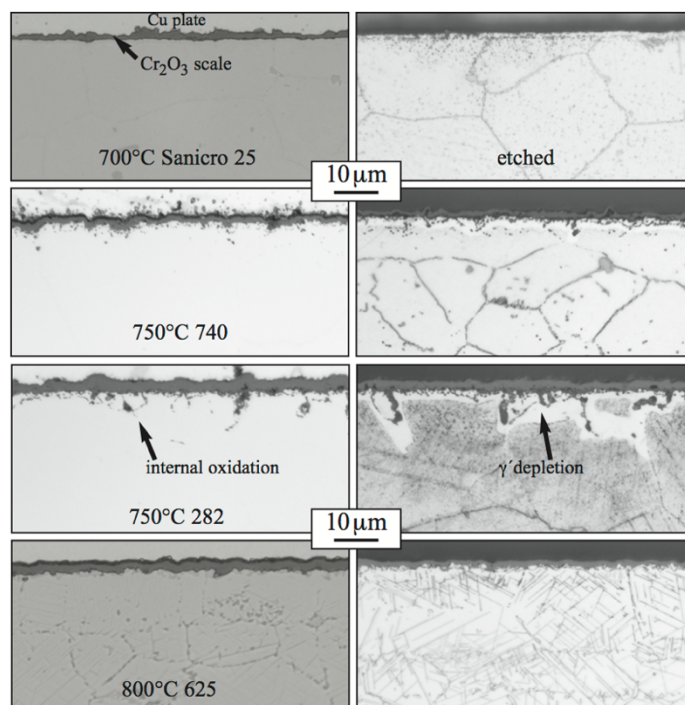

Figure 13. Examples of the additional information gleaned from etching the specimens.
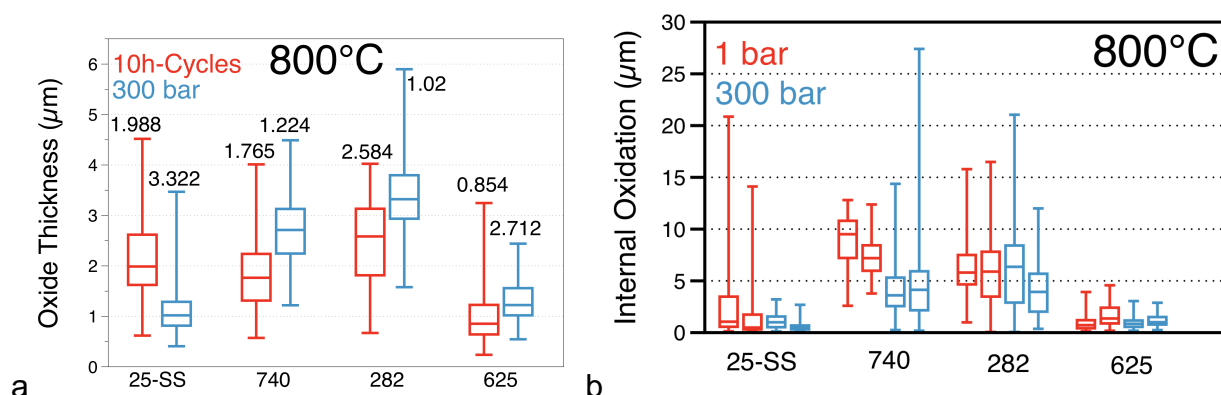
Figure 14. Oxide thickness measurements for the specimens exposed at 800°C. The median value is noted for each alloy as the centerline of the box bounded by the 25% and 75% values. The whiskers note the maximum and minimum values.

for carbides, several specimens were examined by scanning electron microscopy with energy dispersive spectroscopy (SEM/EDX), without being able to identify any particular carbide structures. If present, they may be too small to image. Figure 15 compares the cross-sections after cycling for 1000 h at 800°C in 1 bar IG CO_2 and dry air. In both cases, the internal oxidation looked similar, especially the PS Ni-base alloys 740 and 282. Thus, most of the internal oxidation observed is likely due to oxide formation. However, as a worst-case measurement, the depth of these precipitates was assumed to be similar to any internal carburization. The metric for this subtask was that all of the rates fall below the 10^{-4} $\mu m^2/s$ metric. The highest values measured were 5 x 10^{-5} $\mu m^2/s$ at 800°C so all the measured specimens fell below the metric. While the internal oxidation in some of the images, particularly at 800°C, may seem detrimental, at the current rate of formation it will not significantly affect long-term performance. A similar conclusion was reached in a previous study of 740 and 282 in air, humid air and steam at 800°-900°C [Pint 2015b].
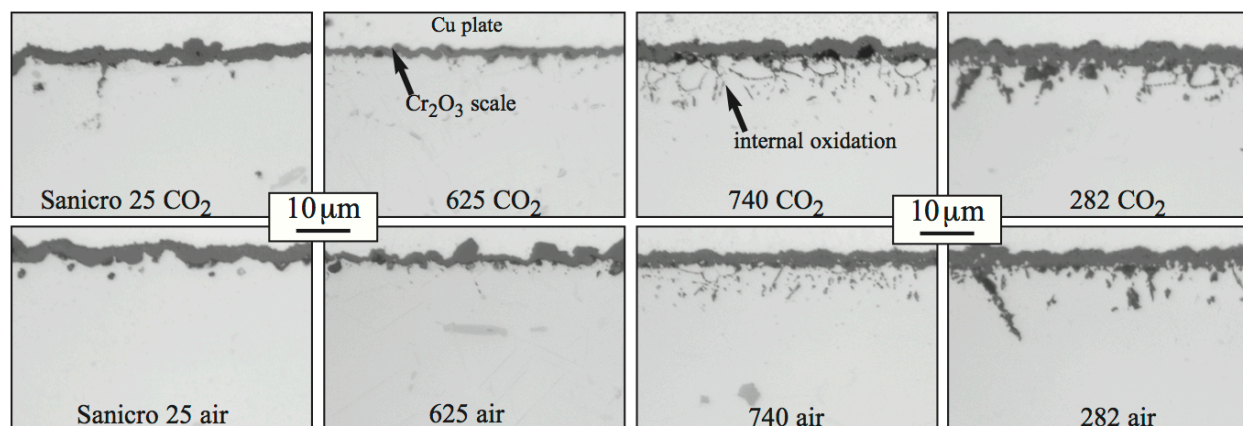

Figure 15. Light microscopy of polished cross-sections of each alloy exposed for 1,000h (100 x 10-h cycles) in 1 bar IG CO_2 and dry air at 800°C.

Subtask 1.3.3: Begin modeling work by analyzing the Arrhenius relationship of the measured parabolic rate constants at 700°-800°C and use results at 700° and 800°C to predict rate at 750°C.

This task was the initial modeling task with a goal of applying the Arrhenius relationship to the data sets at 1 and 300 bar. The dashed lines in Figure 16 were calculated using only the 700° and 800°C rate constants at 1 and 300 bar. Figure 17 plots the measured values at 750°C with the calculated values. Only alloy 625 at 300 bar met the success criteria of being within one standard deviation of the measured value. Alloy 625 did not follow a parabolic relationship at 700°C in 1 bar so no prediction could be made. The results of this subtask suggest that more sophisticated modeling tools will be needed such as a reservoir (Cr consumption) model [Quadakkers 1994, Duan 2016].

Phase 1 milestone:

Develop an initial version of the lifetime model using input data from the 20,000 h of experimental data generated in CO₂ at 700°-800°C during the first year of the project; with the model, predict the reaction rate constant at 750°C within ±1 σ of the average rate measured from the experimental work. Complete a Failure Mode Effect Analysis to quantitatively assess the strengths and weaknesses of each of the candidate alloys with the goal of predicting those most likely to achieve a 30-year lifetime under CSP duties, with acceptable error bars, when accounting for corrosion and mechanical properties.

Cumulatively, ~160,000 h of testing was completed in Phase 1. The model prediction using an Arrhenius relationship was not particularly successful with only 625 at 300 bar fitting that model. Because of the rapid attack of Sanicro 25 at 700°C in both conditions, there appeared to be a change in mechanism between 700°C and the higher temperatures. Thus, Sanicro 25 would not be expected to fit an Arrhenius model.

A Failure Mode Effect Analysis (FMEA) should take into account mechanical properties and corrosion resistance to account for the major high temperature failures. Fatigue is
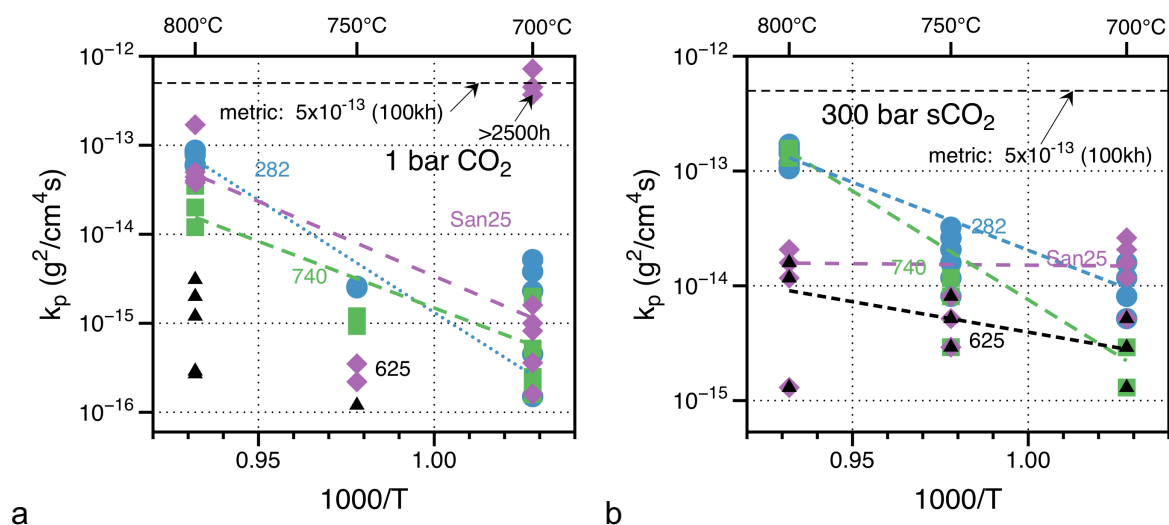

Figure 16. Arrhenius plots with the curves calculated using only the 700° and 800°C rates for this subtask.
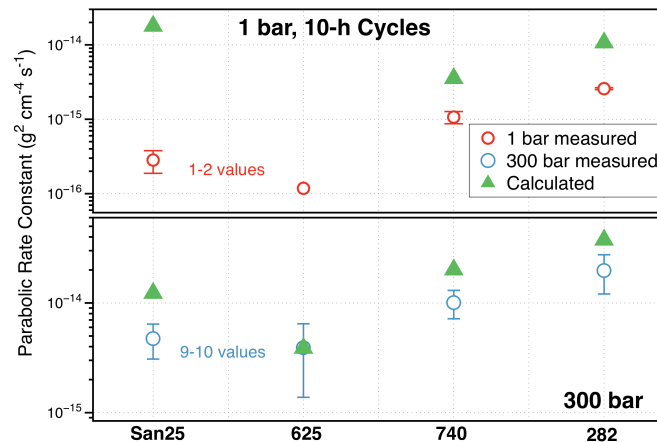
Figure 17. Comparison of the measured and calculated values for both test conditions at 750°C.

also, a concern including high and low cycle fatigue as well as thermal fatigue. However, fatigue testing is scheduled to be conducted in Phase 3. Figure 18 shows relative mechanical properties for 740 and several ASME boiler and pressure vessel (BPV) code qualified alloys. Haynes 282 is not yet code qualified but estimated values are shown. The creep properties should be superior to 740 because the higher fraction of γ' strengthening phase [Pike 2008]. Alloy 625 should be slightly weaker than alloy 617 in Figure 18 and Sanicro 25 should fall in between 617 and 347HFG. Table 2 summarizes a first attempt at a FMEA based on mechanical failures by creep at high temperature, yield (tensile strength) at lower temperature, and oxidation resistance. Based on its superior mechanical properties, 282 appears to be favored while Sanicro 25 had the lowest score because of its lower strength and rapid oxidation at 700°C (see Figure 9a). One advantage for Sanicro 25 should be a much lower cost than the PS Ni-base alloys and 625. However, cost was not included in the average score in Table 2.
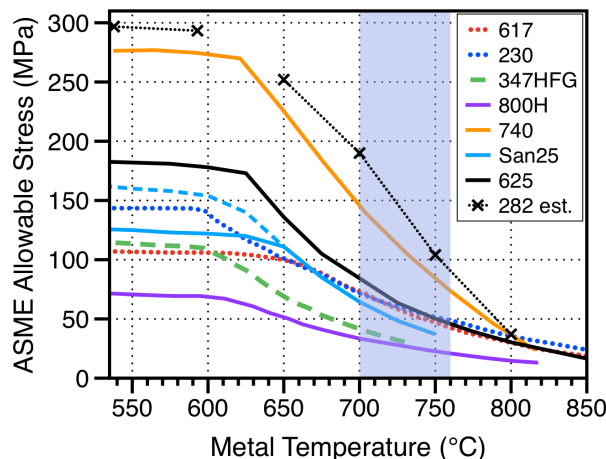

Figure 18. ASME BPV code allowable stresses as a function of operating temperature for several Fe- and Ni-base alloys. Data from deBarbadillo [2014] and Pint [2006].

Table 2. Failure Mode Effect Analysis summary

Alloy	Oxidation	Tensile	Creep	Average	Fatigue	Cost
San25	4	4	4	4.0	–	10
625	10	6	6	7.3	–	8
740	9	9	9	9.0	–	6
282	8	10	10	9.3	–	6

Task 2.1 Conduct testing in carbon dioxide environment

In year 2, the project generated long-term data at 750°C with the same four alloys shown in Table 1.

Subtask 2.1.1: Conduct 500-h cycle testing at 750°C in sCO₂

Results at 750°C and 300 bar IG sCO₂ were extended to 6,000 h in Phase 2. All of the results for this experimental condition are summarized in Subtask 3.2.1.

Subtask 2.1.2: Conduct creep rupture testing at 700°-800°C in sCO₂

This subtask was conducted at Brayton Energy, LLC (BE) in a rig previously constructed with DOE funding, Figure 6a, and described in subtask 1.2.2. For the 740 and 282 tubing, the wall thickness was reduced to minimize the gas pressure needed for the experiments, Figure 6b. This was not necessary for the weaker alloy 625 and 25 tubing. As noted above, Phase 2 testing was focused on longer (500–1000 h) duration experiments (i.e. lower stress levels) and a larger number of specimens were fabricated but, due to time constraints and welding issues with alloys 625 and 282, the number of specimens per condition was typically 3. Figure 19 shows the results of the rupture
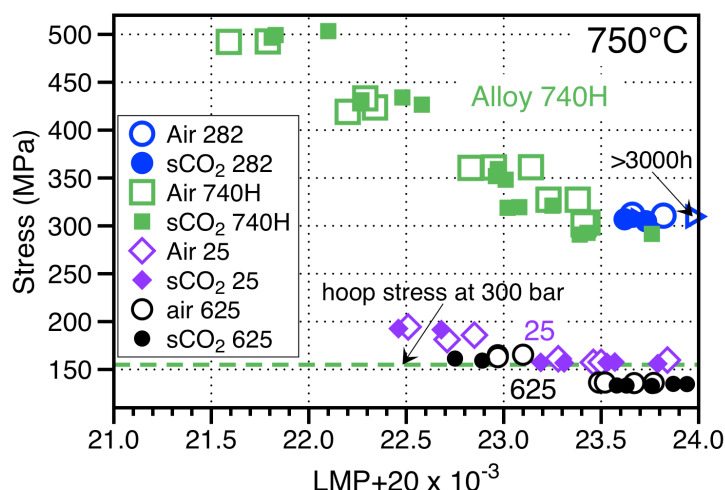

Figure 19. Larson Miller Parameter (LMP) calculated for each rupture versus the applied hoop stress is shown for the sCO₂ and pressurized air experiments. Since the 625 and 25 specimens overlapped, an offset is used to clearly show the data. The hoop stress at 300 bar is shown for the wall thickness of the alloy 740H specimens.

experiments and illustrates the much greater strength of alloys 740H and 282 compared to 625 and 25 as the stress levels used to obtain failure in <2000 h were much higher for the PS alloys. Due to problems with welding, only a few 282 specimens were tested to rupture and additional 740H specimens were added to the test matrix. Several specimens continued to be tested during Phase 3 and two 282 specimens are still in test. In general, there was no effect of environment on the rupture lifetime for any of the materials

Subtask 2.1.3: Conduct 10-h cycle testing at 750°C in CO$_2$

Cyclic experiments were conducted to simulate the CSP duty cycle at 750°C in 1 bar IG sCO$_2$ and were extended from 1,000 h to 7,500 h in Phase 2. All of the results for this condition are summarized in Subtask 3.2.3.

Task 2.1.4 Conduct 500-h cycle testing at 700°C in sCO$_2$

Based on the results shown in Figure 9a, it was decided to continue the 700°C/300bar test for 1,000 h to see if a similar acceleration in mass gain would occur for the alloy 25 specimens. Figure 20 shows the mass gain data for the two additional cycles conducted in Phase 2. Two of the six specimens of each alloy were sectioned in Phase 1 and the remaining four specimens were continued for an additional 1,000 h exposure. No strong acceleration in mass gain was seen in 300 bar IG CO$_2$. Instead all of the alloys showed a slight decrease in the parabolic rate constant at longer times. Based on this result, it appears that thermal cycling does play a key role in degradation in CO$_2$ for alloy 25. Protective behavior was observed in the 500-h cycles at 700°C to 2,000 h while Fe-oxide began to form after 1,500 h of cumulative exposure in 10-h cycles. A similar result was observed at 750°C.
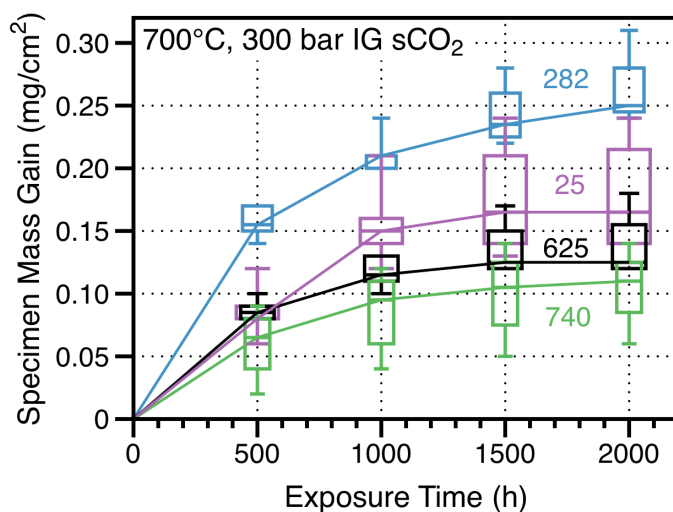

Figure 20. Specimen mass gain during 500-h cycles at 700°C in 300 bar IG CO$_2$. Four specimens of each alloy were continued in the experiment.

Task 2.2 Modeling and Characterization

This is the key task in terms of characterizing the reaction product and developing the lifetime model.

Subtask 2.2.1: Characterize specimens exposed to high and low pressure CO_2 to correlate mass change data with microstructural observations such as reaction product thickness and depth of metal affected.

This subtask involved the metallographic analysis of numerous specimens exposed at 1 and 300 bar from Subtasks 2.1.1 and 2.1.3. The final results from those tasks are summarized together in Subtask 3.3.1. A few examples are provided of data generated in Phase 2. Figure 21a shows EDX maps of alloy 25 after the accelerated attack shown

in Figure 9a. The thick duplex oxide formed after 4,000 h at 700°C is typical of steels exposed to mixed oxidant environments [e.g., Meier 1982]. The outer layer typically forms by Fe transport outward and contains little or no Cr. Apparently due to the high levels of Ni and Cr in this alloy, Table 1, the outer oxide also appeared to contain some Ni. The inner oxide also was contained Ni but it appears that a dense, Cr-rich oxide has reformed at the metal-oxide interface. The Cr map also shows Cr enrichment at the alloy grain boundaries. For comparison, Figure 21b shows the scale formed after 4,000 h at 750°C in dry O_2. A dense Cr-rich oxide was present. In both cases, Nb-rich precipitates were observed in the alloy. The C enrichment appears to be associated with debris in the interfacial voids (arrows).

Figure 22a compares the 1,000 and 2,000 h exposures in 300 bar IG sCO_2 at 700°C for subtask 2.1.4. Because of the lower exposure temperature, all of the reaction products are thin and difficult to image by LM. As expected, the scales are slightly thicker after the longer exposure. The alloy 25 specimen did show a few areas with slightly thicker oxide but based on the low mass gains in Figure 20, these areas were not extensive. Figure 22b shows oxide thickness measurements for the specimens in Figure 22a. The median oxide thickness values (line in each box) increased slightly with time.

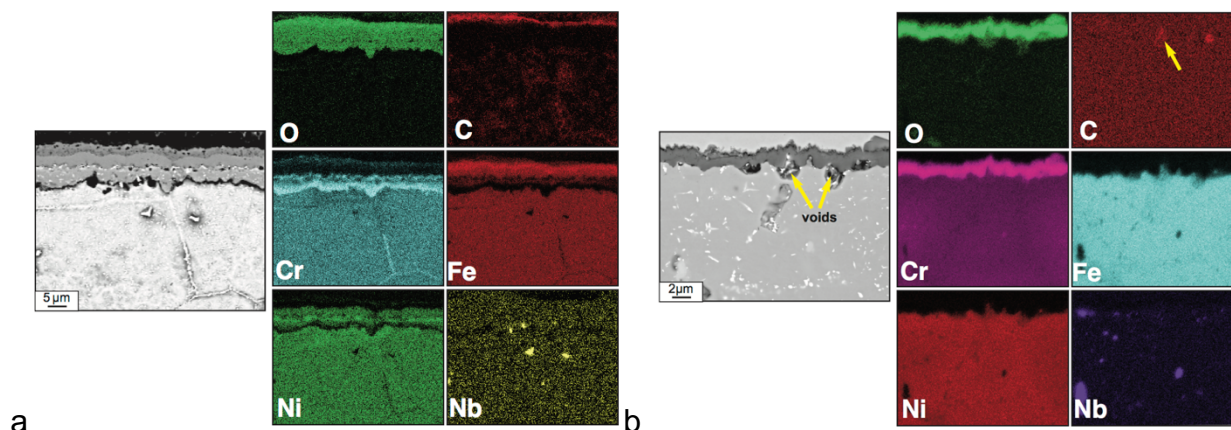a   b

Figure 21. SEM image and associated EDX maps of alloy 25 exposed for 4,000 h (400 x 10-h cycles) at (a) 700°C in 1 atm IG CO_2 and (b) 750°C in 1 atm, dry O_2.
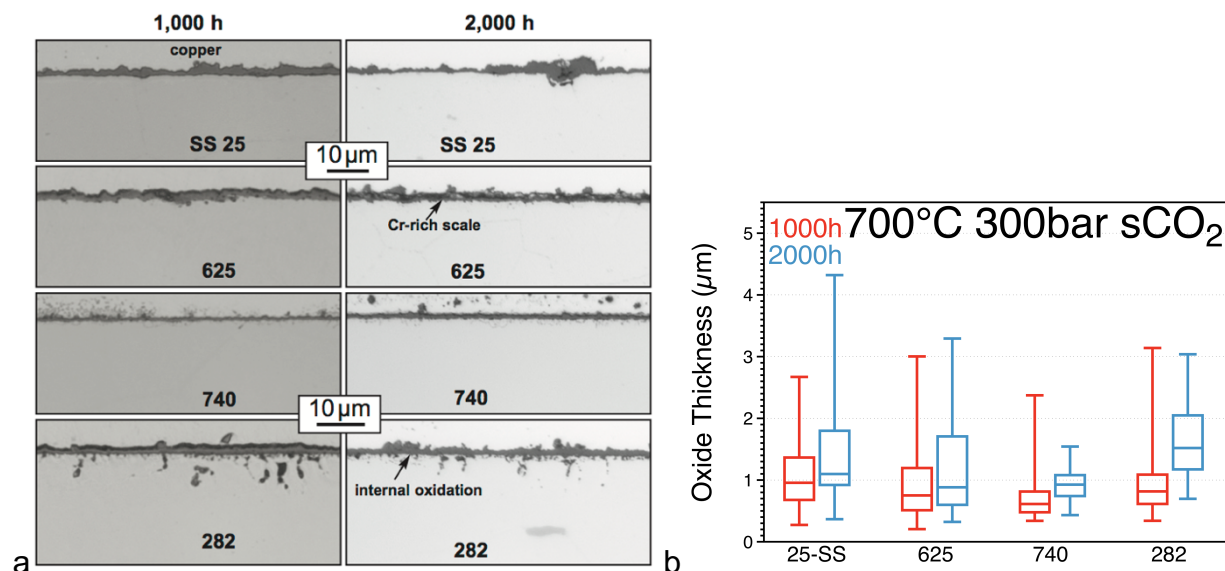
Figure 22. (a) Light microscopy of polished cross-sections of each alloy exposed at 700°C for 1,000 and 2,000 h (using 500-h cycles) in 300 bar IG sCO$_2$. (b) oxide thickness measurements for the specimens in (a).

Because of the thin reaction products, higher resolution characterization was pursued using transmission electron microscopy (TEM) with specimens made by the focused ion beam (FIB) lift out technique. Because of the accelerated attack observed at 700°C, alloy 25 was sectioned after exposure to 300 bar sCO$_2$ at 700°C for 1,000 h, Figure 23a. The major observation was a line of Cr-rich carbides observed beneath the recrystallization (rxn) zone in the metal adjacent to the Cr-rich oxide scale in the sCO$_2$ environment. A similar rxn zone was observed for the specimen oxidized in air for 1000 h at 750°C, but these carbides were not observed [Pint 2018a]. In scales formed in
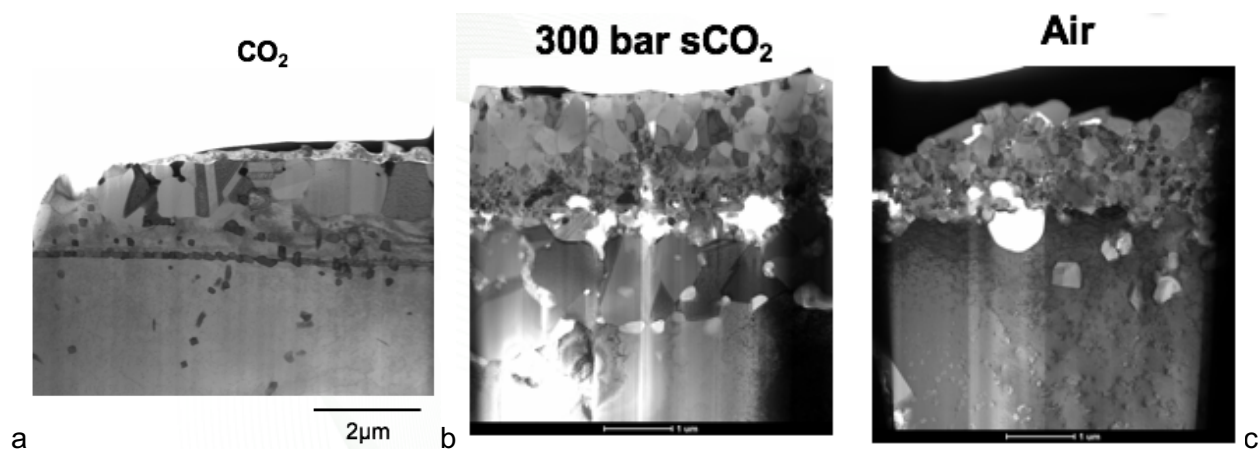

Figure 23. Bright field STEM images of the scale formed (a) on alloy 25 exposed for 1,000 h at 700°C in 300 bar sCO$_2$ and on alloy 282 exposed for 1000 h at 750°C in (b) 300 bar sCO$_2$ and (c) ambient laboratory air [Pint 2018a].

sCO$_2$ and air, TEM/EDX detected C in the scale. Thus, it was concluded that TEM characterization was not able to conclusively identify C in the oxide from the sCO$_2$ environment. Subsequently, these specimens were characterized using x-ray photoelectron spectroscopy (XPS), a more surface sensitive characterization technique. However, no C enrichment was observed by XPS for the sCO$_2$ specimen compared to the air-exposed specimen.

Figures 23b and 23c compare 282 specimens exposed at 750°C for 1,000 h in 300 bar sCO$_2$ and in air. A similar comparison was published for alloy 625 [Pint 2018a]. There was no indication of any internal C-rich precipitates in either alloy after sCO$_2$ exposure. In both cases, the Cr-rich oxide scale formed in sCO$_2$ appeared to be slightly thicker than that formed in air. The oxides formed on alloy 282 are more complex due to the internal oxidation and incorporation of Ti and Al into the scale. In both air and sCO$_2$, there appeared to be void formation at the metal-scale interface. Figure 24 shows TEM EDX maps of the scale formed on alloy 282 in sCO$_2$. The O and Al maps show that the internal oxides are primarily alumina. Titanium appears to be enriched both at the gas interface and the metal-oxide interface of the Cr-rich oxide scale. The C map shows some areas of enrichment. However, the air oxidation specimen also showed similar features. The Si map also shows some enrichment near the metal-scale interface.

Because TEM was not able to find C in the oxide or metal, further characterization was pursued using GDOES. Figure 25 shows the GDOES profiles of Cr and C for alloy 25 and 740H specimens. None of the alloys showed significant C enrichment [Lance 2018]. In many cases, Cr depletion was observed and associated with a C *depletion* near the surface. This has been shown to be related to the Cr-C thermodynamics [e.g. Jalowicka 2015]. In some cases, there was a C peak near the metal-oxide interface but the amount of C was still relatively minor. Higher C peaks were observed for the 700°C sCO$_2$ specimens but represented very little C ingress [Lance 2018].
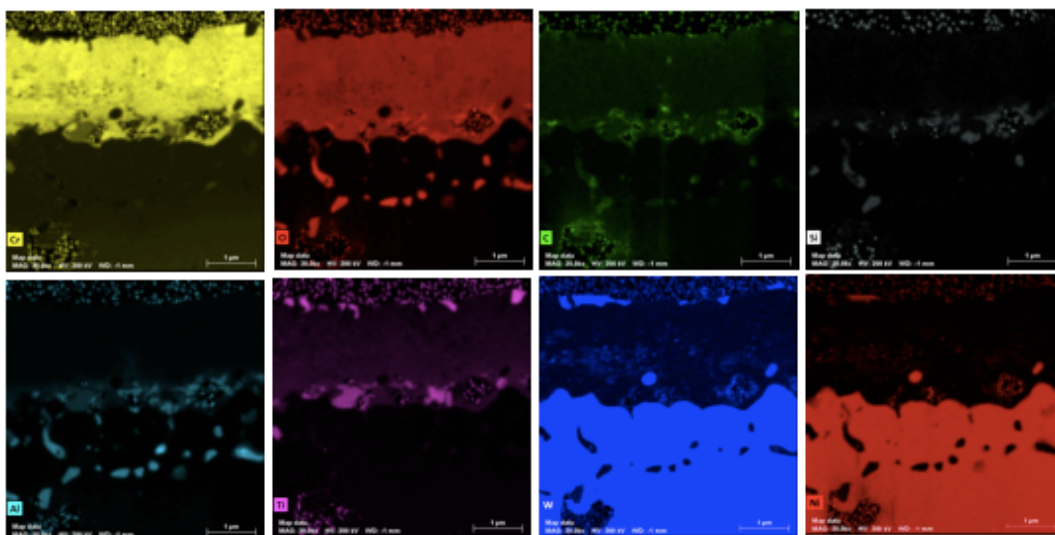

Figure 24. TEM EDX maps of the scale formed on alloy 282 after 1,000 h at 750°C in 300 bar IG CO$_2$ [Pint 2018a].
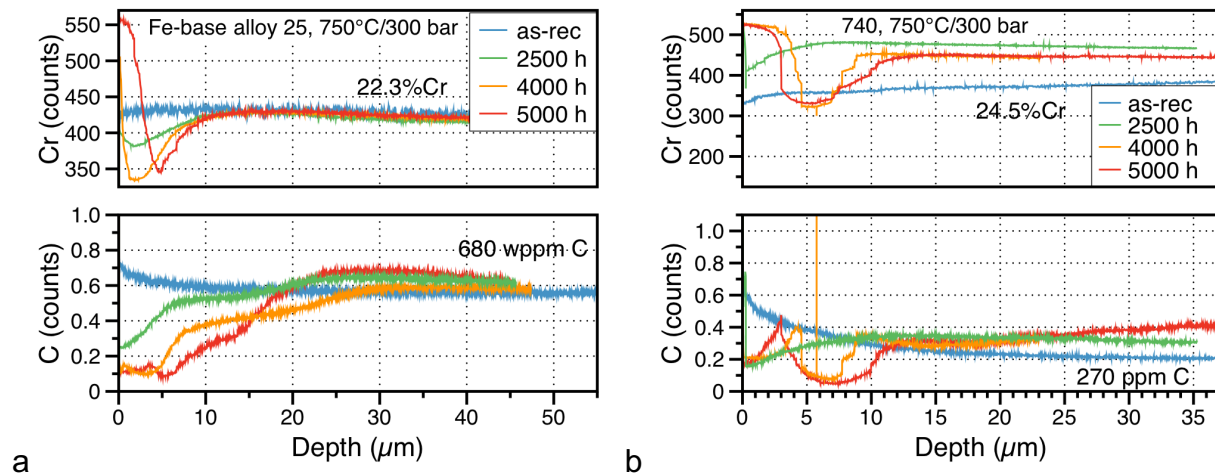
a   b

Figure 25. GDOES profiles in as received material and after three different exposures in 300 bar sCO₂ at 750°C for (a) 25 and (b) 740 [Pint 2018e].

Finally, C ingress is often associated with case hardening of the near-surface region. To assess this possibility, hardness testing was conducted on specimens of 25 and 282 after exposures in air and sCO₂ at 750°C for 1,000 and 2,500 h, Figure 26. Different loads (200-1000 g) were used to vary the penetration of the indenter into the substrate. For the lowest load (200g), it was sometimes not possible to observe the indent into the oxide scale. For both alloys, there was some indication of surface hardening after 1,000 h. However, no differences were observed for the 2,500 h comparisons between air and sCO₂. These results do not suggest that a hardened layer was growing with time in the 282 and 25 specimens exposed to sCO₂.
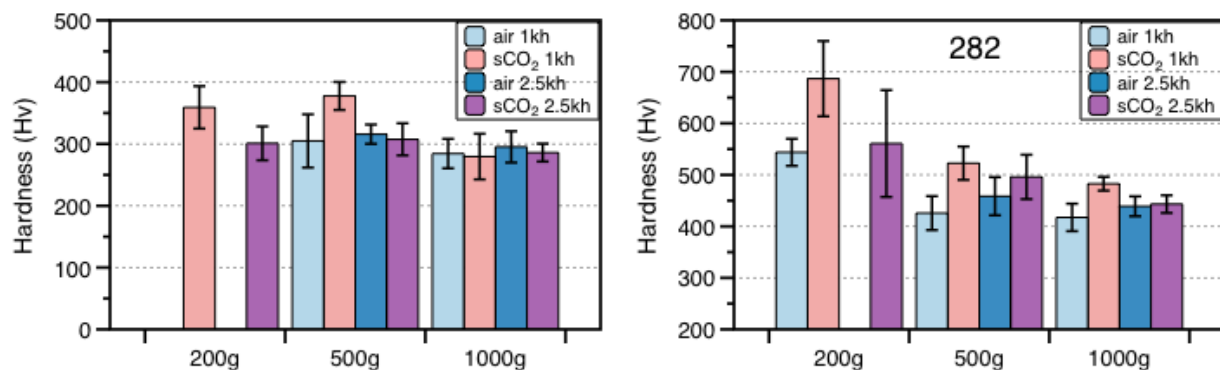

Figure 26. Hardness measurements after laboratory air and 300 bar sCO₂ exposures at 750°C (a) alloy 25 and (b) alloy 282.

Subtask 2.2.2: Continue lifetime modeling work by selecting an established modeling strategy based on the data generated in Task 2.2.1.

This subtask was designed assuming there would be internal carburization, particularly during longer term observations. Without any evidence of internal oxidation, the depth of internal oxidation in 300 bar sCO$_2$ at 750°C was used as a surrogate. The results calculated after Phase 3 will be shown in Subtask 3.3.2. In general, the degradation rates appear so low that any model will yield the result that the degradation is not an issue for 30 year CSP service at 750°C.

Task 2.3: Conduct two surveys of companies that design and manufacture sCO$_2$ CSP systems and alloy manufacturers followed by teleconferences to discuss the feedback.

Two conference calls were conducted with industry on Dec 13, 2016 and July 27, 2017. The December call updated the industry participants on the Phase 1 results. A materials survey followed to update Table 2 and additional categories were added based on the feedback. Most of the feedback was qualitative and the modified rankings are shown in Table 3. A second call was held in July 2017 and input was solicited on possible changes in the work scope for Phase 3. Ultimately, DOE SETO decided not to substantially modify the SOPO for Phase 3.

Table 3. Materials ranking based on industry feedback.

Alloy	Tensile	Creep	Corrosion	Fatigue	Cost	Availability	Fabricability	Total
Sanicro 25	7	4	7	7	7	4	7	43
Alloy 625	7	7	10	7	4	10	10	55
Inconel 740H	10	10	10	4	4	4	4	46
Haynes 282	10	10	10	4	1	4	4	43

Phase 2 milestone:

Select and populate a predictive lifetime model using the relevant data generated during the cumulative 400 kh of experiment time during the first two years of the project and use the model to predict the extent of reaction (e.g. depth of metal affected) after 5,000 and 7,000 h exposures within ±1σ of the extent of attack measured with the experimental work. Update the analytical hierarchy evaluation process with industry feedback to quantitatively assess the strengths and weaknesses of each of the candidate alloys with the goal of predicting those most likely to achieve a 30 year lifetime under CSP duties, with acceptable error bars, when accounting for corrosion and mechanical properties. This assessment will take into consideration mechanistic explanation for the observed performance.

Cumulatively, ~415,000 h of testing was completed in Phase 1 and 2 for the original test matrix of 700°-800°C at 1 bar (10-h cycles) and 300 bar (500-h cycles) in IG CO$_2$. Adding on the additional experiments in air, O$_2$ and 1 bar IG CO$_2$, the cumulative total exceeds 700,000 h. The results of the materials evaluation are shown in Table 3. The

numbers and categories were based on industry feedback. Alloy 625 showed the highest score because of its high scores for cost, availability and fabricability.

Regarding the modeling, as noted above in subtask 2.2.2 on modeling, the model result seems to be values that are too small to affect performance. If the values for internal oxidation are used, the measurements are simply too scattered to yield anything useful as it is difficult to measure small values. Figure 27 shows the experimental data for the 750°C 300 bar sCO$_2$ conditions and the curve fits with and without the 5,000 data. Table 4 shows that in only one case (alloy 282) was the 5,000 h prediction within one standard deviation of the measured median value.

Task 3.1 Obtain industry feedback to assess the project and determine how the lifetime model may be modified to benefit CSP stakeholders.

A teleconference was conducted in June 2018 with ~12 participants and the presentation was later distributed to 18 people. For the impurity levels in Task 3.2.4, there was feedback from 2 companies that 50 ppm O$_2$ and 50 ppm H$_2$O appeared to be reasonable levels to target for these experiments at 750°C. The modeling strategy used by EPRI [Kung 2018] to predict the effect of oxide thickness on heat exchanger pressure drop was discussed. An additional modeling request suggested by one company and seconded by another was to estimate the effect of the oxide formation on heat transfer.

Task 3.2 Complete testing in carbon dioxide environment

Subtask 3.2.1: Complete 500-h cycle testing at 750°C in sCO$_2$

For this subtask, 8 specimens of each alloy continued testing in 300 bar IG sCO$_2$ at 750°C using 500-h cycles (continued on from Subtask 2.1.1). Figure 28a shows the data as box and whisker plots with the whiskers noting the minimum and maximum values and the box marked by the 25% and 75% values. The median values for each box are connected by a solid line. For characterization (Subtasks 2.2.1 and 3.3.1), specimens were removed periodically for characterization and 4 specimens of each
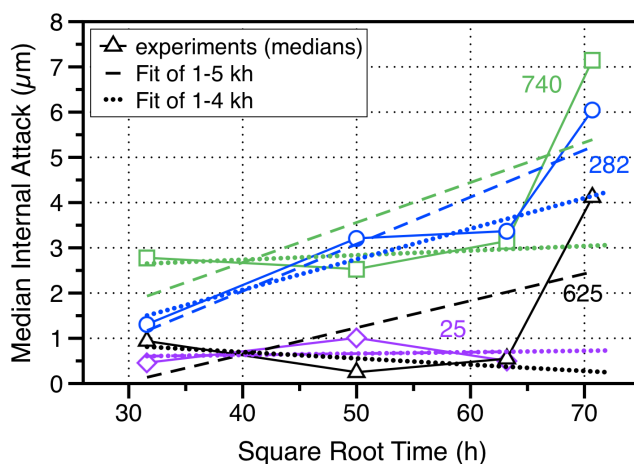

Figure 27. Parabolic fits with all of the data and fits not using the 5,000 h data in order to model 5,000 h behavior.

Table 4. Results of the Phase 2 milestone for 300 bar sCO$_2$ exposures at 750°C

Alloy	5kh expt μm	sigma	5kh Predict	success
25	n.d.		0.7	n.d.
625	4.1	0.82	0.3	No
740	7.2	3.8	3.1	No
282	6.1	2.9	4.1	Yes

alloy completed the 10,000 h exposure. The rate constants were generated by plotting the specific mass change versus the square root of time [Pieraggi 1987] and plotted in Figure 28b along with the values measured at 700° and 800°C in Task 1.2.1. For alloys 740H and 282, the mass gains were higher due to the internal oxidation of Al and Ti (Table 1) as well as the incorporation of Ti into the Cr$_2$O$_3$ scale, which has been found to accelerate the oxide growth [Ennis 1985, Brady 2006, Pint 2015b]. For the alloy 625 specimens in Figure 28a, the mass gains were low. For the Fe-base alloy 25, there was an initial higher increase in mass followed by a rate similar to alloy 625. All of the specimens maintained a rate constant below the metric of 5 x 10^{-13} g^2/cm^{4}s. The project evaluation criterion for this subtask was that the linear spallation rate be less than 10^{-9} g/cm^{2}s. Since none of the specimens showed evidence of spallation, that metric was met.

In addition to 300 bar experiments, 1 bar IG CO$_2$ experiments also were authorized to determine the effect of CO$_2$ pressure. The mass change data are summarized in Figure 28a by a dashed line connecting the median values of 3-8 specimens of each alloy. The mass gains were very similar for most of the alloys. The largest difference was for the alloy 25 specimens where the initial mass gain in 1 bar IG CO$_2$ was much lower.
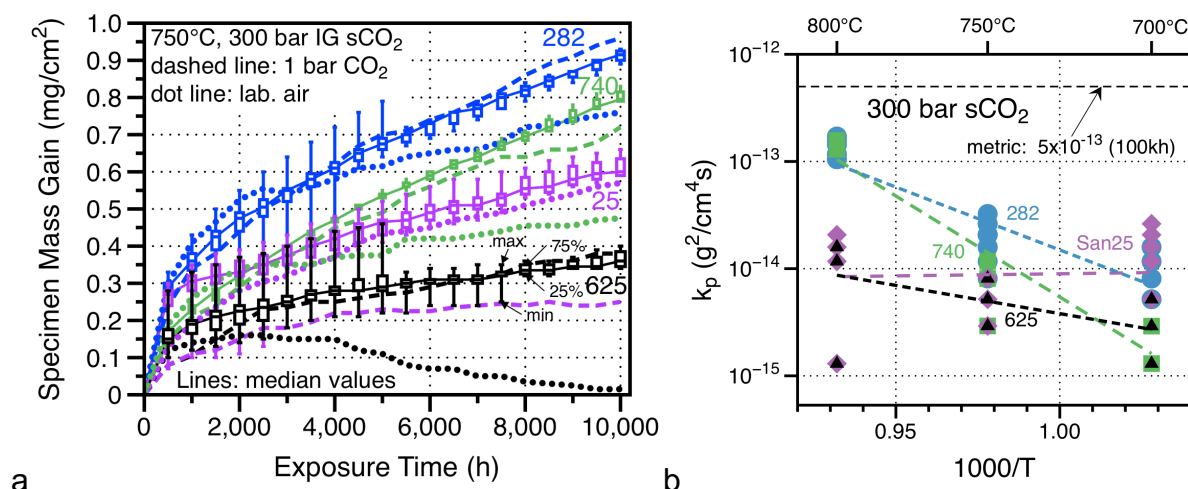

Figure 28. (a) Specimen mass gain as a function of exposure time at 750°C using 500-h cycles in 1 bar IG CO$_2$ (dashed line), 300 bar IG sCO$_2$ (solid line and box/whiskers) and laboratory air (dotted line); the lines connect median values of 6-10 specimens at each condition [Pint 2019a], (b) Arrhenius plot of the rate constants measured in 300 bar IG sCO$_2$.

Finally, a set of specimens was exposed in laboratory air at 750°C using 500-h cycles to provide a baseline for characterization in a non-CO_2 environment. The mass change data are summarized in Figure 28a by a dotted line connecting the median values of 2-8 specimens of each alloy. While the alloy 25 specimens continue to gain mass at a rate similar to that in sCO_2, the other specimens have generally begun either mass loss (alloy 625) or very low mass gains (alloys 740 and 282). The parabolic rate constants calculated from the median values in each condition are shown in Table 5.

Subtask 3.2.2: Complete creep-fatigue testing at 700°-800°C in sCO_2

This task at Brayton Energy, LLC (BE) was intended to test 740H, 282 and 625 specimens similar to those used for creep testing, Figure 6b. The fatigue cycle was isothermal with a nominal stress of 41.4 MPa (6 ksi) with 6 min hold per cycle, a total cycle time of 8 min and an estimated lifetime of 3,000 cycles (~24 days to complete). Figure 29 shows the testing for 740H, which lasted considerably longer than the target time. One specimen of 740H that completed ~6300 cycles in CO_2 was stopped without failure to switch to testing in pressurized air. Unfortunately, those experiments in pressurized air required even longer times to failure, which suggests an environmental effect, Figure 29. The average lifetime in air was 10086±1142 cycles and the average lifetime in CO_2 was 4287±1680 cycles, a factor of 2.3X drop in the lifetime. Again, one specimen was stopped at 12,970 cycles without failing. BE was going to begin testing of 625 specimens with a higher stress than originally planned to cut the target testing time to 13 days. However, no data has been reported at this time.

Subtask 3.2.3: Complete 10-h cycle testing at 750°C in CO_2

This tasked continued on from Subtask 2.1.3 to simulate the CSP duty cycle by exposing specimens for 10-h thermal cycles at 750°C in flowing, 1 bar IG CO_2 (100 cc/min flow rate) followed by 10 min cooling out of the furnace in air to < 30°C. Two cyclic rigs were used in Phases 2 and 3. The rigs are run for one week intervals (16 cycles) and the specimens are weighed each week. Figure 30 summarizes the mass change results for this subtask. Similar to the 300 bar sCO_2 experiments, the 282 specimens initially showed the highest mass gains. The 625 specimens showed a small linear mass loss in mass after an initial increase. Most striking, the alloy 25 specimens exhibited an accelerated rate of mass gain, similar to the Year 1 observation at 700°C, Figure 9a. As a result, it was decided to stop testing the alloy 25 specimens and focus on the Ni-based alloys. One alloy 25 specimen was run to 7,500 h. One specimen gained 1.5 mg/cm² before being stopped after 400, 10-h cycles.

Table 5. Calculated parabolic rate constants (g^2/cm^4s) using 500-h cycles for 5,000-10,000 h in five different environments at 750°C.

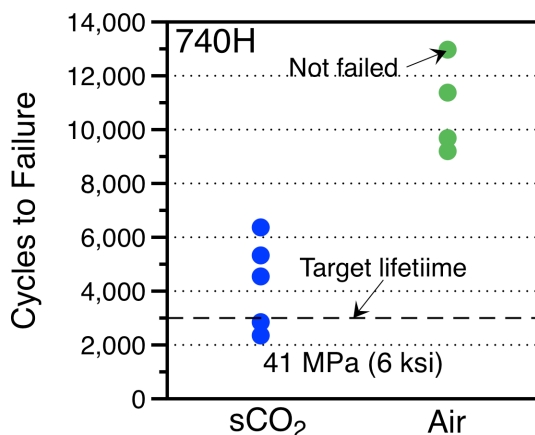| Alloy	IG sCO₂	IG CO₂	RG sCO₂	RG CO₂	air
25	5.6E-15	1.6E-15	1.8E-14	1.6E-15	8.45E-15
625	1.7E-15	3.9E-15	6.9E-15	2.3E-15	---
740	1.9E-14	1.7E-14	3.5E-14	2.4E-14	2.79E-15
282	1.8E-14	2.3E-14	3.0E-14	1.6E-14	7.34E-15

Figure 29. Cycles to failure for 740H tube specimens pressurized at 750°C with air or CO₂. Each cycle consisted of an 8min hold at 41 MPa followed by depressurizing.

The performance criteria for this subtask was for the spallation rate to be below 10^{-9} g/cm²s for specimens exposed in CO_2. Only the 625 specimens showed a mass loss with an average rate of 5.4 x 10^{-12} g/cm²s. In fact, the rate is so low that it is not likely due to oxide scale spallation. Spallation usually requires sufficient oxide thickness for the strain energy in the oxide to exceed the interface adhesion [Evans 1995]. With these small mass gains, the oxides are <1 µm thick and should not spall. Also, an inspection of the specimens after exposure did not show evidence of scale spallation.
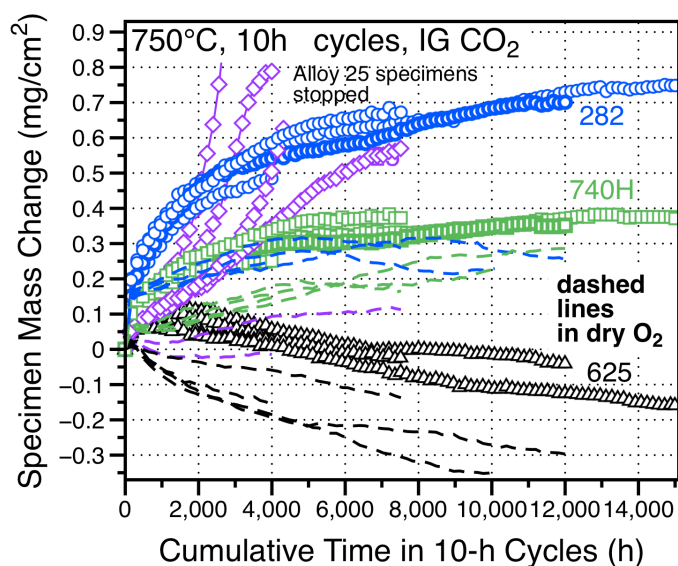

Figure 30. Specimen mass gain during 10-h cycles at 750°C in 1 bar IG CO_2 (symbols) and dry O_2 (dashed lines) [Pint 2019a]. Four specimens of each alloy were exposed to CO_2 and removed after 4, 7.5, 12 and 15 kh.

To better understand these results, companion experiments were started in Phase 2 in flowing O_2. Figure 30 shows the mass change data for the specimens in this experiment using dashed lines. Groups of specimens were removed after 1, 4, 7.5, 10 and 12 kh. Compared to the specimens exposed in CO_2, the mass changes were typically lower. In particular, the alloy 25 specimens did not show signs of accelerated attack after the longest exposure of 7,500 h. The low values and particularly the consistent mass losses for the alloy 625 specimens, suggests scale spallation. However, as noted above, the scales are thin and there was no visual evidence of scale spallation. Previously, it has been suggested that the mass losses for alloy 625 are due to Mo evaporation.

An additional experiment using 1-h cycles at 750°C in IG CO_2 with 10 min cooling in air between cycles also was conducted, Figure 31. To fill the seven rig spots, two specimens of each Ni-based alloy and one specimen of alloy 25 were exposed for 4,000 cycles (125 cycles/week). The observed mass gains were somewhat lower for the alloy 740 and 282 specimens but very similar for the 625 specimens in 1-h and 10-h cycles. The alloy 25 specimen showed an increased mass gain at about the same time as the specimens exposed in 10-h cycles, Figure 31. This result suggests that a certain number of cycles is not needed to trigger this increased attack associated with the formation of Fe-rich oxide. Instead, it may be related to a level of Cr depletion at ~1500 h of exposure. However, no similar acceleration has been observed in 500-h cycles, Figure 28a.

Subtask 3.2.4 Testing in impure sCO₂ at 750°C/300bar

An additional task was added to study the corrosion rate with controlled additions of O_2 and H_2O relevant to an indirect-fired cycle. ORNL had built a rig for testing high impurity
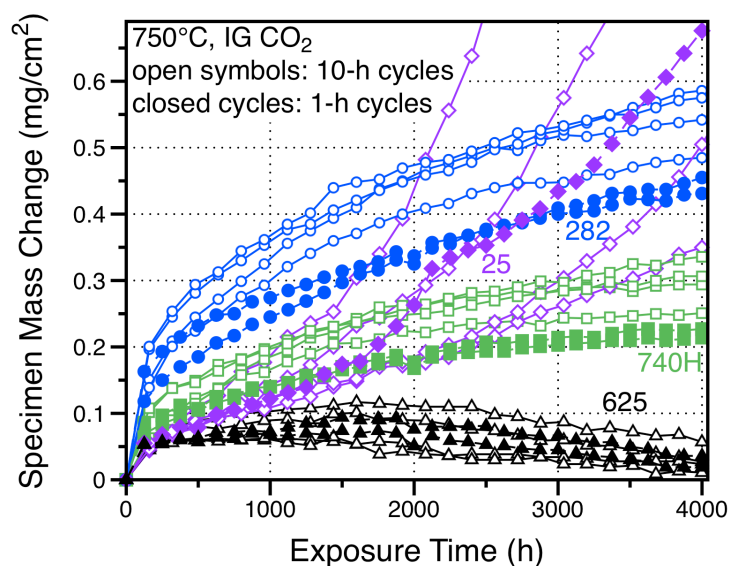

Figure 31. Comparison of specimen mass gain during 1-h (solid symbol) and 10-h cycles (open symbols) at 750°C in 1 bar dry O_2.

levels [Pint 2019b] relevant to direct-fired Allam cycles, where O_2 and H_2O levels can be 1% or more [Kung, 2016]. The impurity levels selected for this experiment were 50 ppm O_2 and 50 ppm H_2O as discussed with industry in Task 3.1. A second autoclave was modified for this experiment and included three pumps: the standard sCO₂ pump used for all of the autoclaves, a pump for a mixed CO_2-O_2 gas mixture and a micro-pump for the H_2O. In this case, RG CO_2 was used with <5 ppm O_2 and < 5ppm H_2O. The O_2 and H_2O levels were controlled based on the inputs into the autoclave.

Figure 32 shows the mass change data for 4 specimens run to 2,500 h (5, 500-h cycles) at 750°C/300 bar. The mass gains were very similar to those measured in IG sCO₂, Figure 28a. Since these impurity levels are very similar to the upper bound for IG sCO₂, it is not surprising that the mass gains were similar. The parabolic rate constants in impure sCO₂ were all within a factor of 2 of the values in IG sCO₂ with the rates lower for the Ni-based alloys and higher for alloy 25.

Task 3.3 Modeling and Characterization

Subtask 3.3.1: Complete characterization of specimens exposed to high and low pressure CO_2 to correlate mass change data with microstructural observations.

The 750°C reaction products were primarily characterized by examining polished cross-sections. For example, Figure 33 shows one of the specimens exposed for 2,500 h at 750°C/300 bar in IG sCO₂ and in RG sCO₂ with additions of 50 ppm O_2 and 50 ppm H_2O. Consistent with the mass change data in Figure 32, the oxides appear very similar in thickness on each of the alloys. One of the goals of the project was to remove specimens at equivalent times so that comparisons could be made among the various
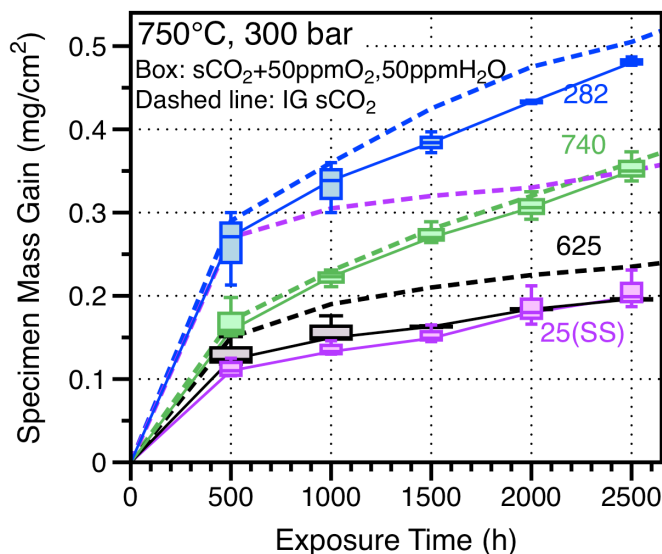

Figure 32. Box and whisker plots of the mass change for 3-4 specimens exposed to 750°C/300 bar sCO₂ with 50ppm O_2 and 50ppm H_2O with the median values connected with a solid line. Median specimen mass change in IG sCO₂ is shown as dashed lines (data from Figure 28a).
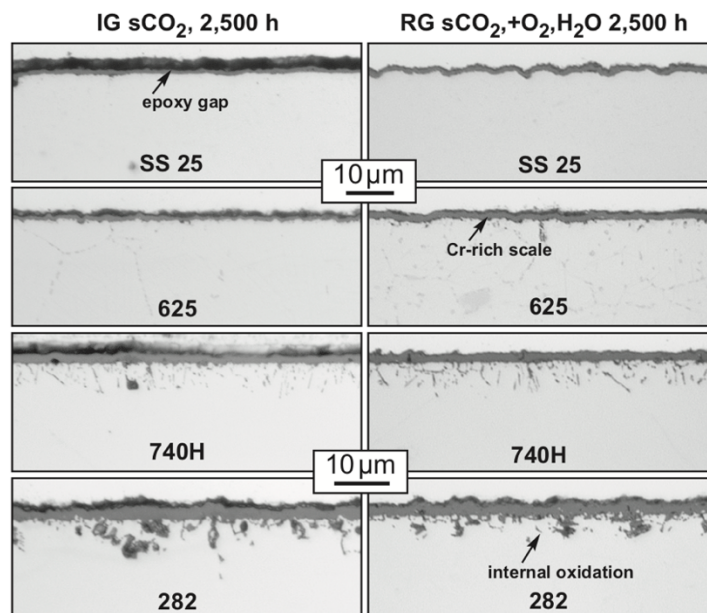
Figure 33. Light microscopy of polished cross-sections for the specimens exposed at 750°C for 2,500 h in 2 different sCO₂ conditions using 500-h cycles.

environmental conditions. Figure 34 gives an example where all of the specimens were exposed for a total of 7,500 h in 500-h or 10-h cycles with and without CO₂. Figure 35 shows examples for 10,000 h exposures in Figure 28a. As reported previously, the alloy 25 and 625 specimens typically show thin Cr-rich external oxide scales with little or
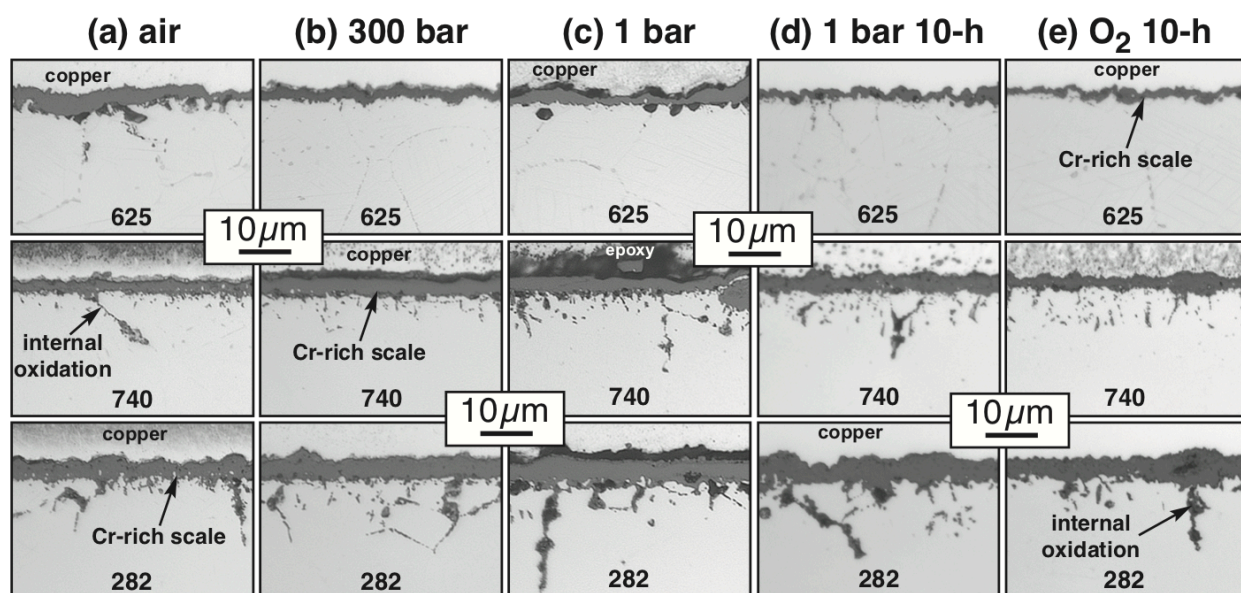

Figure 34. Light microscopy of polished cross-sections for the three Ni-based alloys exposed at 750°C for 7,500 h in 5 different conditions using 500-h cycles.
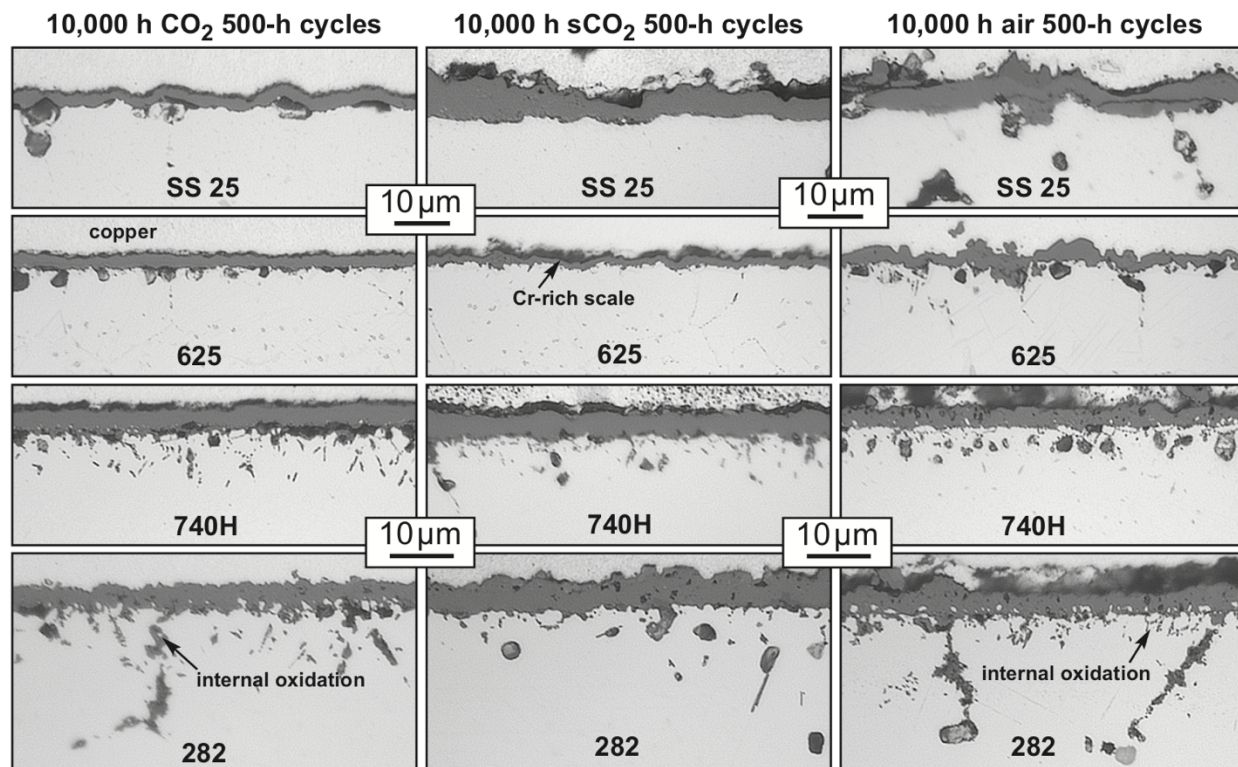
Figure 35. Light microscopy of polished cross-sections for the specimens exposed at 750°C for 10,000 h in 3 different conditions using 500-h cycles.

no internal oxidation after these various exposures. In contrast, the alloy 740 and 282 specimens show increasing internal oxidation of Al and Ti with exposure time and typically a thicker surface oxide. All of the specimens were Cu-plated in order to protect the oxide during polishing and to facilitate measuring the oxide thickness. However, sometimes the adhesion is not good. In Figure 33, there is a gap that makes the oxide look thicker on the alloy 25 specimen. Figures 34 and 35 reinforce the mass change results that there is little difference between air or O_2 oxidation and CO_2 or sCO_2 behavior. The internal oxidation is nearly unchanged, independent of exposure conditions. This observation is quantified in Figure 36 for the Ni-based alloys exposed in three conditions using 500-h cycles: laboratory air, 1 bar IG CO_2 and 300 bar IG sCO_2. The results for oxide thickness and depth of internal attack were similar in each case for the Ni-based alloys.

Figure 37 compares the reaction products formed after 4,000 h in dry O_2 and IG CO_2 exposed using 10-h cycles and IG CO_2 using 1-h cycles. There is an obvious effect of CO_2 for alloy 25 as reflected in the accelerated attack observed in Figures 30 and 31. The thicker reaction product was similar to that formed at 700°C and characterized in Figure 21a. A classic two-layer structure formed with an outer layer rich in Fe and inner layer rich in Cr. For the Ni-based alloys in Figure 37, there was very little effect of environment or cycle frequency, consistent with the mass change. Figure 38 shows the time series of specimens exposed in 10-h cycles out to 15,000 h for the Ni-based alloys.
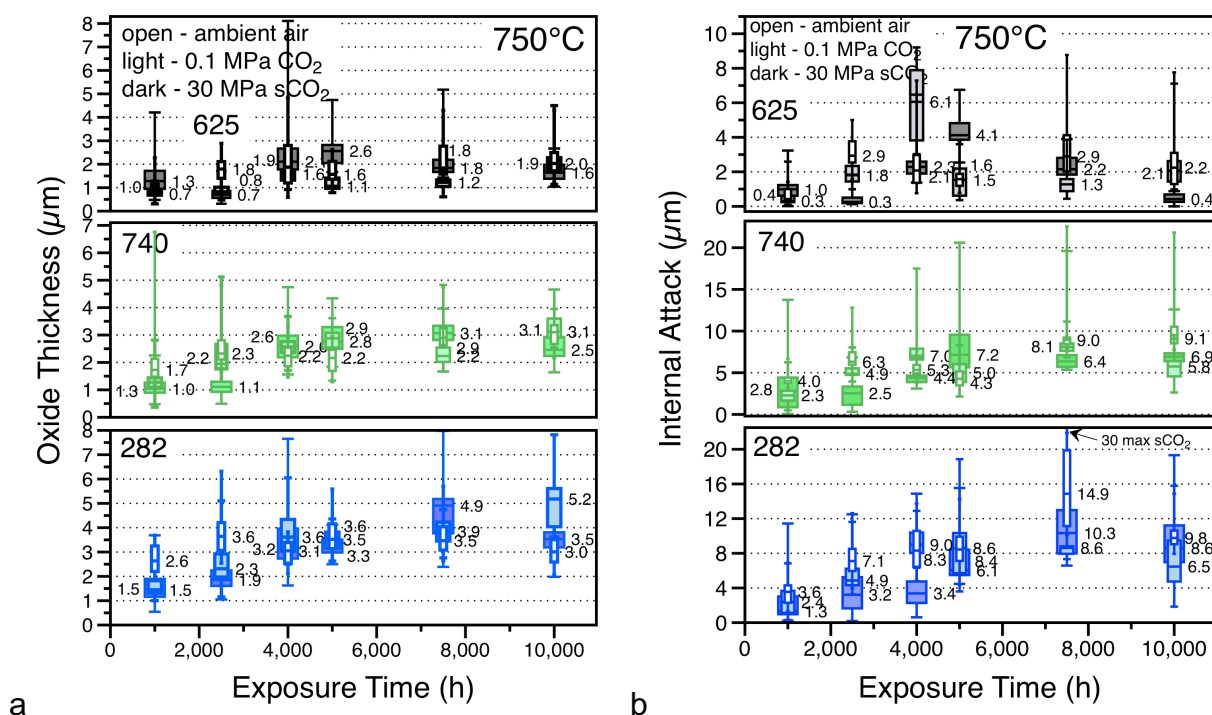
Figure 36. Box and whisker plots of oxide thickness and internal oxidation for specimens exposed at 750°C in 1 and 300 bar sCO₂. The whiskers mark the max./min. values.

The oxide thickness and internal oxidation are quantified in Figure 39 for O_2 and IG CO_2. The thinnest reaction products were observed for the alloy 625 specimens and
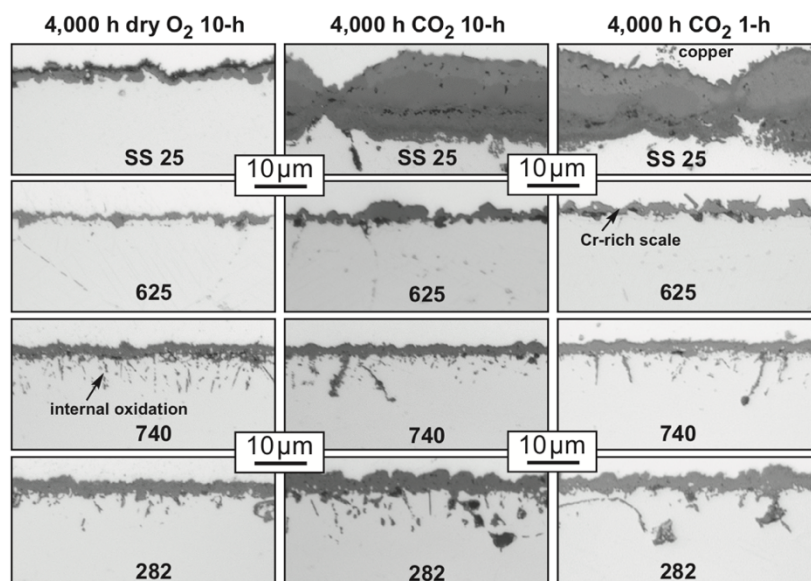

Figure 37. Light microscopy of polished cross-sections for the specimens cycled at 750°C for 4,000 h in 1-h and 10-h cycles.
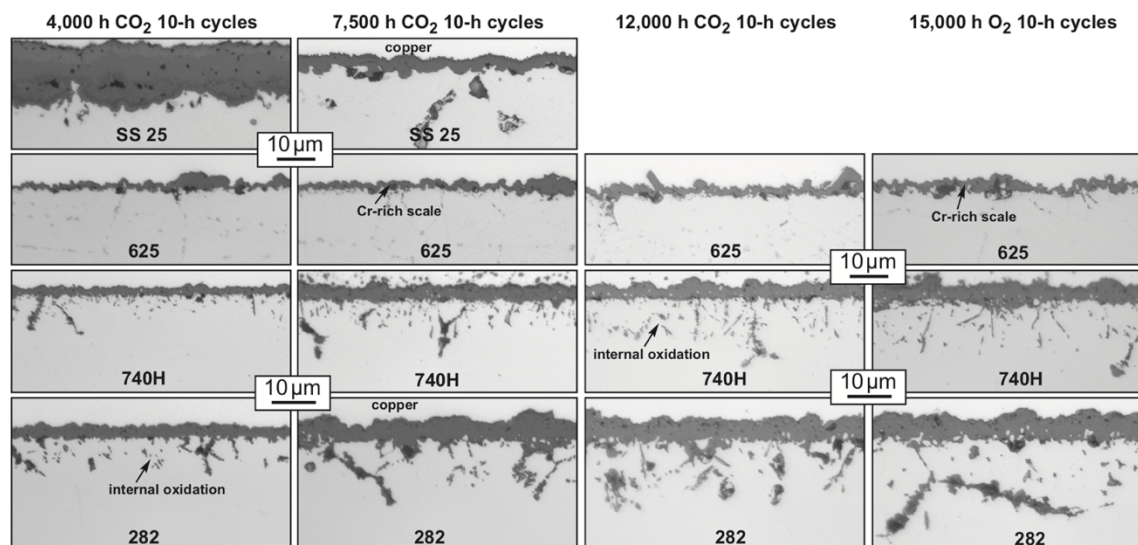
Figure 38. Light microscopy of polished cross-sections for the specimens exposed at 750°C using 10-h cycles in 1 bar IG sCO$_2$.

the thickest oxide and internal attack were observed for the alloy 282 specimens. Little difference was observed between the two environments and the 10kh sCO2 results are shown for reference in each case.

Figure 39. Box and whisker plots of oxide thickness and internal oxidation for specimens exposed at 750°C in 10-h cycles. The whiskers mark the max./min. values.

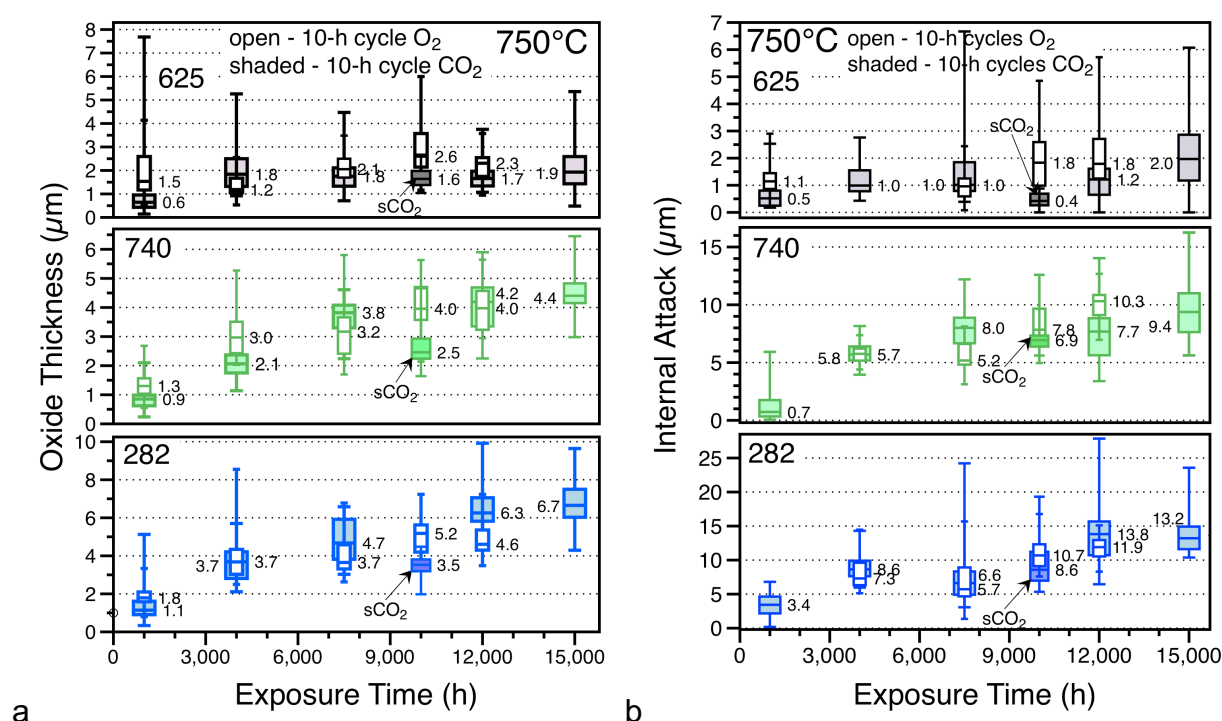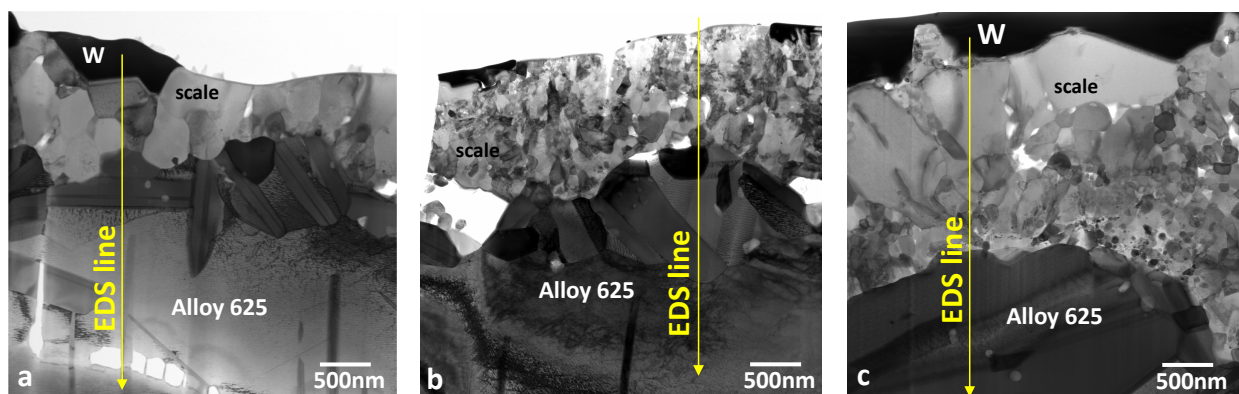Figure 40. BF-STEM cross-sectional images of the scales formed on alloy 625 after 5,000 h at 750°C in (a) laboratory air, (b) 0.1 MPa CO_2 and (c) 30 MPa sCO_2 [Pint 2018b].

In order to further assess the effect of pressure, scanning transmission electron microcopy (STEM) specimens of alloy 625 specimens were examined after exposures at 5,000 h exposures in 1 and 300 bar IG CO_2 as well as in laboratory air. Figure 40 shows bright field (BF)-STEM images of the scale cross-sections after 5,000 h exposures. The grains appear to be larger in the scale formed in air (Figure 40a) and finest in the scale formed in 1 bar CO_2 (Figure 40b). In the area sectioned, the scale formed in 300 bar sCO_2 appears slightly thicker, which is consistent with the measurements, Figure 40c. Again, judging by the area sectioned in Figures 40b and 40c, the porosity in the scale and at the metal-scale interface appear to be higher after exposure in CO_2. EDS line profiles in Figure 41 are from lines marked in Figure 40. As expected, the scales are mainly Cr_2O_3 and contain low levels of Mn with some Ti incorporation. Al in the alloy forms internal oxides. To complicate the analysis, Mo and Nb form precipitates at the metal-scale interface as they are rejected from the reaction front [Chyrkin 2011]. Sputter depth profiles using glow discharge optical emission spectroscopy (GDOES) also did not detect any C enrichment after exposure of this specimen [Lance 2018].

Finally, a further review of all GDOES analysis of Phase 2 specimens did find a higher level of C beneath the scales formed at 700°C in 300 bar sCO_2, particularly for the alloy
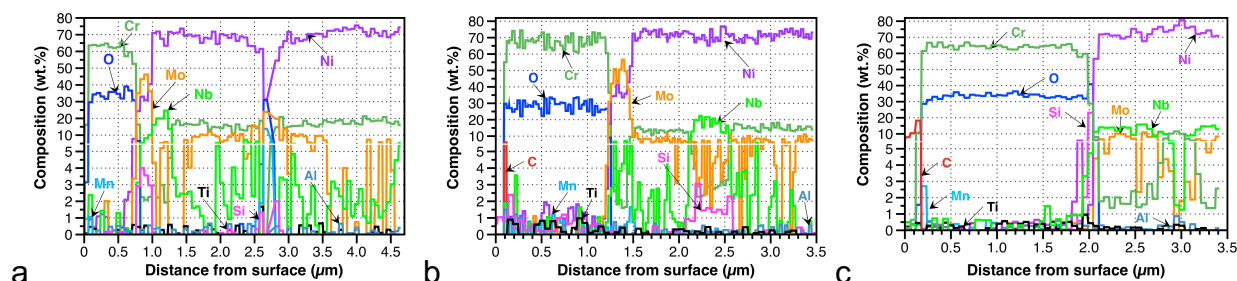

Figure 41. EDS line profiles associated with the images in Figure 41 of scales formed on alloy 625 after 5,000 h exposures at 750°C in (a) laboratory air, (b) 0.1 MPa CO_2 and (c) 30 MPa sCO_2 [Pint 2018b].
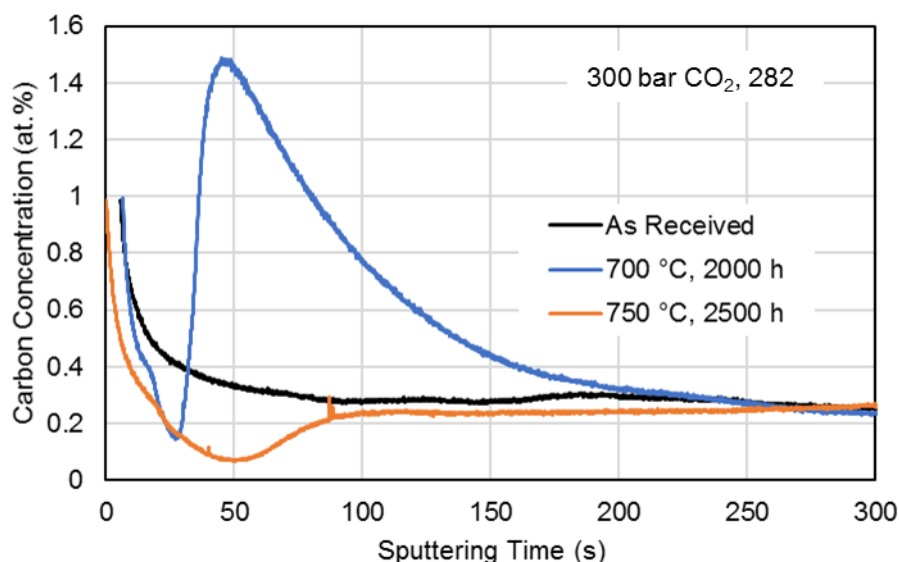
Figure 42. GDOES C concentration profiles for 282 exposed to 300 bar sCO₂ at 700 °C and 750 °C. Also shown is an as received 282 sample for comparison.

282 specimen, Figure 42. However, no similar enrichment was found for any of the 282 specimens exposed to sCO₂ at 750°C [Lance, 2018]. Furthermore, the depth was only a few microns.

Subtask 3.3.2: Complete lifetime modeling work by incorporating the data generated in Task 3.1.

The oxide thickness and internal oxidation depth data were fit to parabolic rates and extrapolated to 100,000 h in order to illustrate that these low rates represent modest (≤40 μm) amounts of attack after long exposures, Figure 43. In Figure 44, the mass change data were fit both parabolically and to a power law (a linear fit on a log-log plot of thickness versus time). The exponent n varied from 0.28 to 0.51 (parabolic behavior is n=0.5) and also had low R^2 values. The alloy 25 data were best fit in two stages.

Another avenue for modeling may be to model the Cr depletion (i.e. Cr consumption) using a reservoir-type Cr consumption model [Quadakkers 1994, Duan 2016]. Cr-depletion profiles for the candidate alloys were calculated by numerically solving the Fick's laws and employing average diffusion coefficients for Cr in Ni-base alloys [Pillai 2013]. The experimentally measured oxidation kinetics was employed as a boundary condition at the alloy surface to simulate the oxidation induced Cr loss. Half specimen thickness was used as the computational domain assuming symmetry. This simple procedure gives a quick estimate of Cr concentration at the O\M interface and allows a relatively rapid comparison of residual lifetime for different alloys. However, this procedure does not consider the influence of the chemical interaction between alloying elements on their transport properties. Furthermore, the driving forces for diffusion are governed by the gradients in chemical potential which are strongly influenced by the
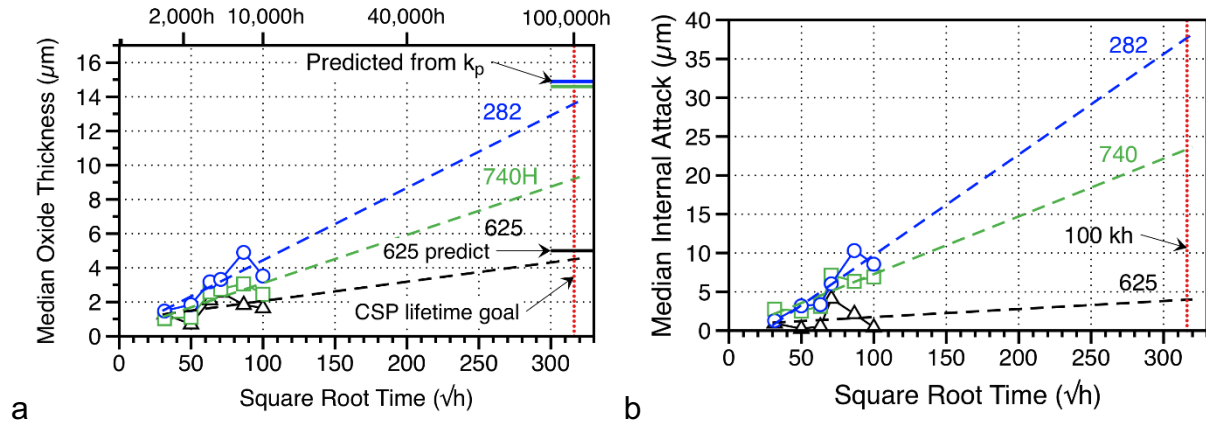
Figure 43. Extrapolation of the (a) oxide thickness and (b) internal oxidation depth data observed at 1,000–10,000 h in 300 bar sCO_2 to 100,000 h assuming parabolic behavior. In (a), the oxide thickness values calculated from the parabolic rate constants are shown.

compositional changes and phase transformations occurring in the alloy.

To demonstrate the applicability of a more sophisticated procedure, the compositional changes in one of the candidate alloys, alloy 625 were predicted by a coupled thermodynamic-kinetic model [Pillai 2015]. The modelling procedure utilizes commercially available thermodynamic data to calculate thermodynamic phase equilibria as a function of temperature and composition and kinetic data to determine the compositional evolution in the alloy. All chemical interactions between alloying elements are considered. The recession of the oxide\metal (O\M) interface due to metal consumption to oxidation is calculated and the computational mesh is accordingly regenerated, thus enabling a more
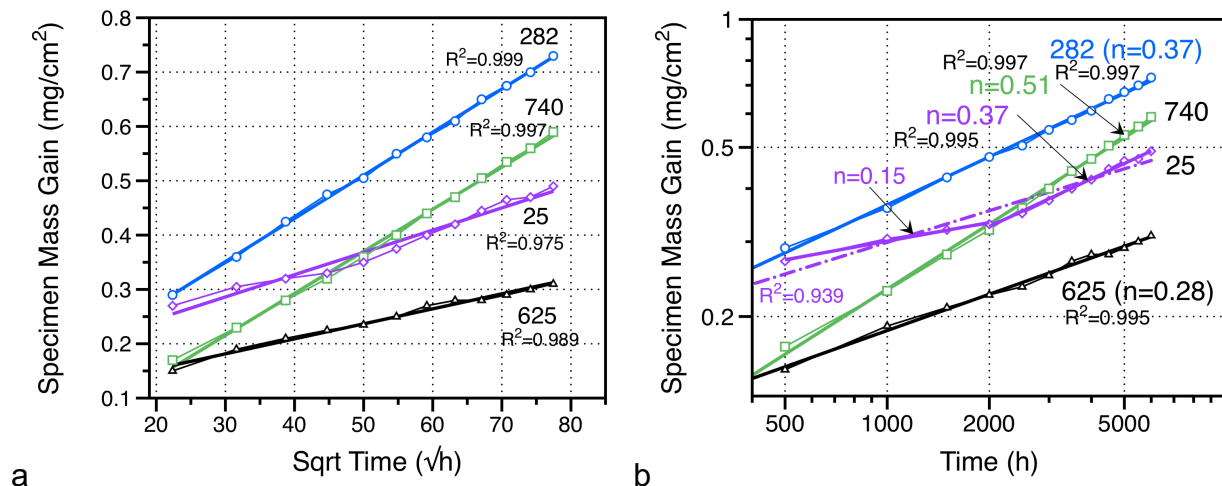

Figure 44. Plot of the median values from Figure 5 at 750°C 300 bar (a) parabolic relationship with square root of time and (b) log-log determination of exponent n where parabolic behavior is n=0.5. The R^2 values are shown.

realistic calculation of e.g. Cr depletion profiles. The thermodynamic database TTNI8 and kinetic database MOBNI2 were employed in the calculations performed for the candidate alloys.

For studying the critical Cr depletion, a protective chromia scale is expected to form on the candidate alloys up to 100,000 h at 750°C based on the extrapolation of the 10 kh exposure data. However, it has been shown previously that a protective external chromia formation can most likely not be sustained below a critical value of Cr concentration at the scale/alloy (O/M) interface. The critical value was given to be 10 wt.% [Pillai 2013, Duan 2016]. The concentration of Cr at the scale/alloy interface is governed by its consumption due to oxidation (oxidation kinetics) and its rate of transport from the alloy to the O/M interface (diffusion coefficient). For the case of parabolic oxidation kinetics, the Cr concentration at the interface is dependent on the initial Cr concentration and the ratio between the oxidation constant k_p and the diffusion coefficient of Cr D_{Cr} in the alloy. In other words, if the oxide scale is not damaged due to spallation or depleted due to moisture induced evaporation of chromia, the interface Cr concentration remains constant [Wagner 1952]. Figure 45 shows the calculated Cr concentration at the O/M interface for a 100,000 h exposure between 700-850°C. Protective oxidation behavior in terms of the Cr concentration at the O/M interface being above 10 wt.% is expected for the three candidate alloys up to 800°C. However, only alloy 625 will most likely continue to form an external chromia scale at 850°C. It must be considered that these calculations assume that the consumption of Cr continues parabolically up to 100,000 h.

To account for potential spallation of the chromia scales after longer times or due to thermal cycling induced by abrupt shut-down procedures, calculations were performed by assuming additional Cr loss due to spallation of the oxide scales. For the case of 50% higher loss, the Cr concentration at the O\M interface for alloys 740 and 625 was 15 and 14 wt.% respectively but at about 11.5 wt.% was closer to the critical value for alloy 282.
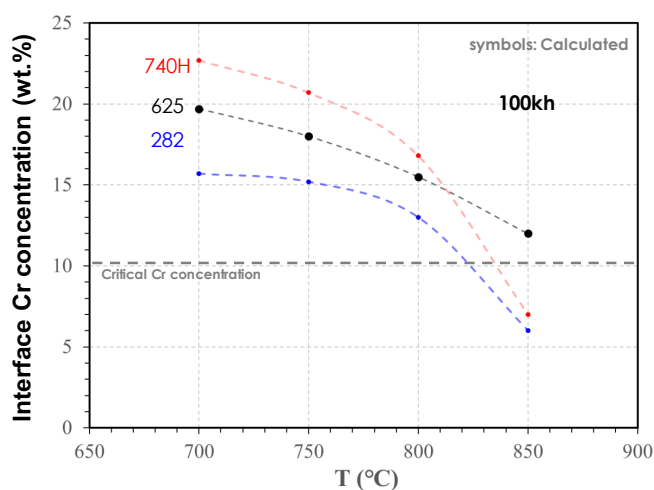

Figure 45. Calculated Cr concentration at the scale\alloy interface for a 100,000 h exposure between 700°-850°C using 500-h cycles.

As mentioned above, a more sophisticated calculation was performed for alloy 625 to predict the microstructural changes occurring during exposure under sCO$_2$ at 750°C. Figure 46 compares the measured (EDS) and calculated Cr concentration profile after exposure in sCO$_2$ for 10000h at 750°C. The model predicted an O/M interface Cr concentration of 14.6 wt.% while the measured concentration was about 14 wt.%. The simpler modelling procedure predicts a value of about 18 wt.% and the deviation from measured values can mainly be attributed to neglecting the influence of chemical interactions between alloying elements on the diffusion coefficient and ignoring the chemical potential driven transport processes.

The calculated evolution of the phases in alloy 625 after 10,000h is compared with a corresponding BSE image in Figure 47. The observed precipitation of the δ-phase at the O\M interface and the formation of a denuded zone beneath the externa oxide scale indicated in the BSE image in Figure 47a have been reported before [Chyrkin 2011]. The model predicts both observed phenomena and the extent of the denuded zone is also correctly predicted (~ 5μm).

There was industry interest expressed in the channel blocking model proposed by EPRI [Kung 2018]. The growth of oxide scales in small flow channels of sCO$_2$ recuperators would result in a reduction of the flow areas of the channels which would consequently lead to pressure drops across the channel. Typically, a 2-5% of reduction in flow area (RFA) is considered acceptable [Kung 2018]. Two circular channels with 0.3mm and 0.9mm ID were considered for the calculations. Oxide thicknesses which would allow an RFA≤5% up to 100,000 h were calculated for both channel sizes from the oxidation rate constants shown in Figure 5b. The time to attain this oxide thickness at 700, 750 and 800°C is plotted in Figure 48. A 0.3 mm ID channel would most probably be too
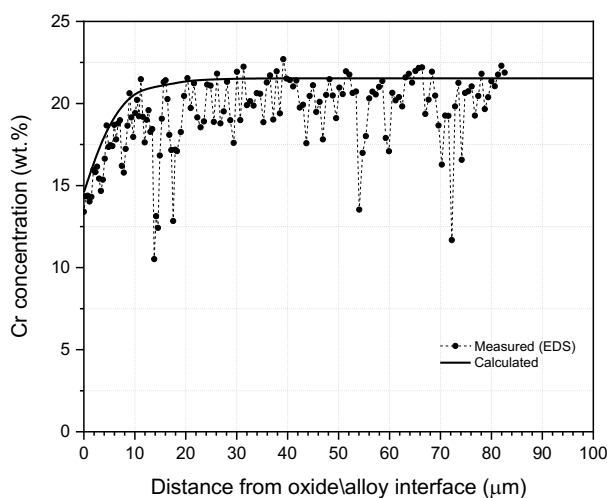

Figure 46. Comparison between the measured (EDS) and calculated Cr concentration at the scale\alloy interface for a 10,000 h exposure at 750°C using 500-h cycles.
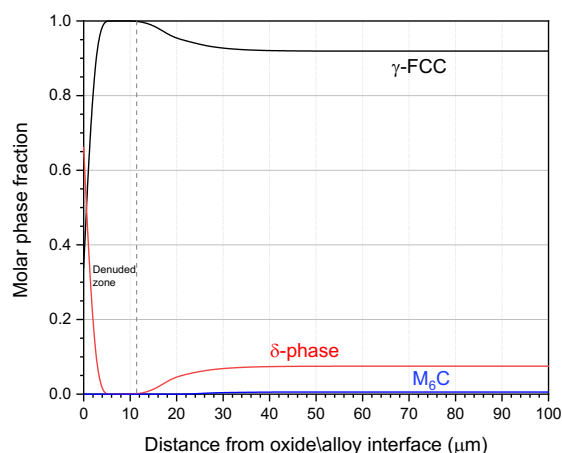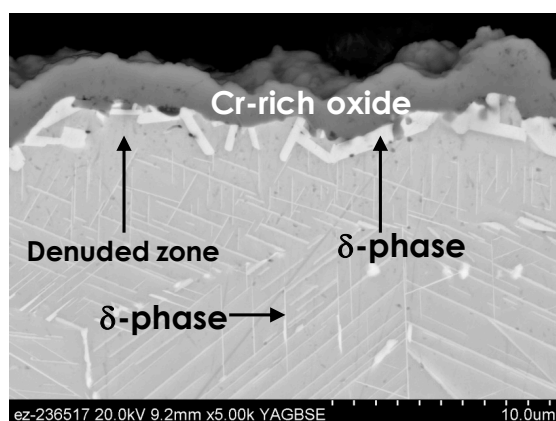
Figure 47. (a) BSE micrograph of cross-section of alloy 625 and (b) calculated phase distribution for a 10,000 h exposure at 750°C using 500-h cycles.

narrow to prevent an RFA≤5% up to 100,000 h at 750°C for all candidate alloys. With a 0.9 mm ID channel, all alloys are expected to satisfy the RFA≤5% criteria for 100,000 h at 750°C and would most likely continue to do so even at 800°C.

As discussed previously, no experimental evidence was found for carburization of alloys 625, 740 and 282 under sCO₂ at 750°C. The driving force for C in the alloy will be governed by the chemical potential gradient of C activity from the O\M interface towards the alloy. The exact value of the C activity at the O\M is difficult to determine and hence

Figure 48. Calculated time to 5% RFA for (a) 0.3 mm and (b) 0.9 mm ID channel at 700, 750 and 800°C.

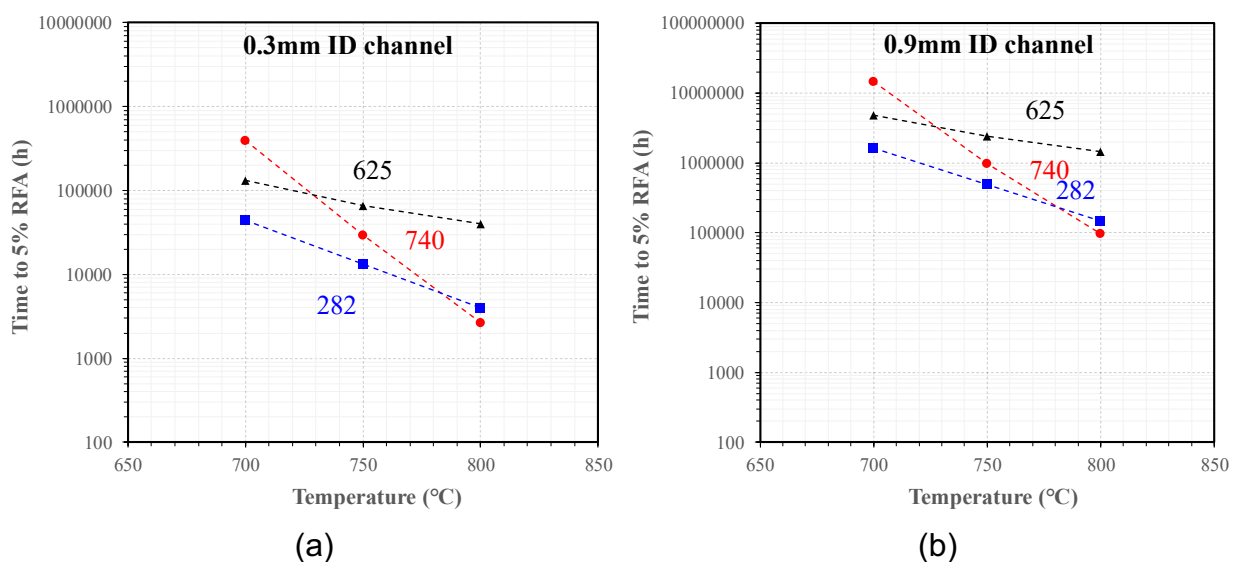diffusion calculations were not performed to model the carburization behavior of the candidate alloys. Thermodynamic calculations were performed for alloy 740 to demonstrate the extent of carbon ingress required to precipitate a significant fraction of carbides. Figure 49 shows a calculated isopleth of a Ni-Cr-C-Co-Al-Ti-Mo-Nb phase diagram at 750°C with constant Co, Al, Ti, Mo and Nb concentrations corresponding to those of alloy 740. The red symbol marks the initial concentration which will be almost on the Cr axis due to the low C concentration and corresponds to the typically observed γ-γ' microstructure of 740 with a few MC-type carbides (M=Ti,Nb). Due to the oxidation induced depletion of Cr in the subsurface region, a higher amount of C is required to precipitate additional Cr-rich carbides. In the case of alloy 740, this corresponds to a C concentration of about 0.3 wt.% which would necessitate significant C ingress. Other compositional changes, such as Al and Ti depletion due to internal oxidation might even push this value higher.

Assuming that C manages to penetrate the external oxide scale, the much faster diffusion velocity of C compared to Cr (about three orders of magnitude) will also mean that C is transported to the specimen center from the sub-surface region. The much higher concentration of Cr in the core might the result in precipitation of new carbides. This hypothesis will be verified in future studies.
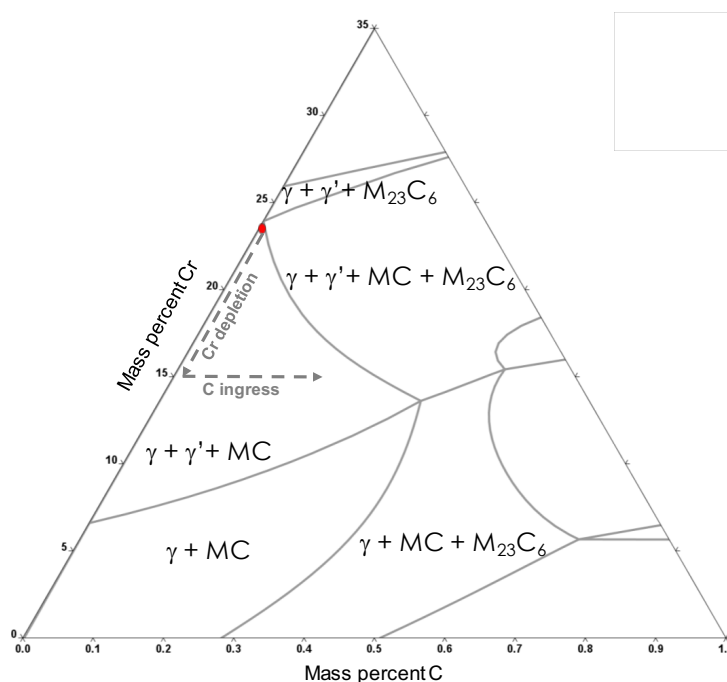

Figure 49. Calculated isopleth of a Ni-Cr-C-Co-Al-Ti-Mo-Nb phase diagram at 750°C with constant Co, Al, Ti, Mo and Nb concentrations corresponding to those of alloy 740.

Final Phase Milestone: Using the cumulative 1,100,000 h of specimen exposure data generated during three years of the project, (1) predict the extent of reaction in sCO_2 after 100,000h for each candidate alloy; (2) identify any debit in expected creep or creep, hold-time fatigue lifetime in the sCO_2 environment; and (3) predict the extent of reaction after 15,000 h within ±1 σ of the extent of attack measured with the experimental work. Rank the performance of each of the candidate alloys using an analytical hierarchy evaluation process and identify any limitations gleaned from the project. Outline multiple CSP industry use cases of the lifetime model based on industry feedback.

The predictions are contained in the previous section. No debit in creep rupture lifetime was identified but Figure 29 indicated a >2X debit in creep fatigue life for alloy 740H specimens. Unfortunately, these experiments took much longer than expected (target lifetime shown in Figure 29) and the 625 specimens began testing in the final month of the subcontract, but no failures were reported before the project ended. No changes in the alloy rankings were proposed for Table 3.

Regarding the use of the model, a final paper based on the results in section 3.3.2 remains to be written in order to communicate the final status of the modeling. In particular, the critical Cr and channel blockage parts were developed in the final months of the project and these may be the most useful aspects.

Significant Accomplishments and Conclusions

More than 1,250,000 h of cumulative testing in industrial grade CO_2 and non-CO_2 environments has been conducted at 700°-800°C in this project on three Ni-based alloys and one stainless steel with the 2nd and 3rd project phases focusing on long-term testing at 750°C for 10-15 kh. These exposures included additional experiments in research grade CO_2 that were cost-shared with a DOE Fossil Energy project. The results have been illuminating both showing low reaction rates for the NI-base alloys at 700°-800°C at 1 and 300 bar and limited carbon ingress, despite the accelerated attack observed for Fe-based alloy 25 in 10-h cycles at 700° and 750°C. The project successfully addressed the question about materials available for >700°C operation in sCO_2. Prior to the project, very little data had been generated for >500 h at >700°C particularly for the precipitation strengthened, Ni-based alloys 740 and 282. Degradation modes hypothesized in the original proposal such as carbon ingress and oxide scale spallation were not an issue. This was good news for the development of sCO_2 technology, but made the modeling task more challenging, particularly in the early stages. Nevertheless, significant progress was made in modeling, especially during the final year of the project and these data will help future lifetime modeling efforts.

Overall, the cyclic oxidation testing showed that the daily thermal cycling of a CSP system should not be a concern for the Ni-based alloys under these conditions. The relatively thin oxide reaction products do not have sufficient strain energy to lead to spallation even when cycled 4,000 times in 1-h cycles. The mechanical property testing of tube specimens at 750°C showed limited impact of the sCO_2 environment on creep rupture lifetime but a >2X debit in creep-fatigue lifetime for the one alloy (740H)

evaluated using an 8 min hold per cycle. The mechanical testing subtask was a challenge to complete within the 3-year time frame because of the uncertainty in predicting the test matrix for experiments where there was no prior data for comparison. Also, multiple industry surveys were conducted of stakeholders to provide feedback to the project and the results of this project are well-known to the sCO₂ community through conference calls and numerous publications and presentations.

The initial work scope was expanded to include 1 bar testing in industrial grade CO_2 and air and O_2, without an increase in project budget. These experiments set a baseline to show that the reaction rates in sCO₂ were not significantly different than those in ambient air or ambient pressure CO_2. The results also suggest that CO_2 pressure is not a significant parameter for compatibility. Similarly, cyclic testing in O_2 showed comparable behavior as the results in CO_2. The accelerated attack observed for alloy 25 specimens did not occur in O_2 and was observed at a similar cumulative time in 1-h and 10-h cycles. Finally, the role of impurities was explored by adding controlled levels of O_2 and H_2O (50 ppm each) at 750°C/300 bar and no change in mass gain or reaction products was observed compared to baseline exposures in industrial grade sCO₂.

The time series of exposures in each condition provided numerous opportunities to draw a link between the mass change measurements and the reaction product thickness with >200 specimen metallographically mounted and analyzed. Advanced characterization techniques such as glow discharge optical emission spectroscopy (GDOES) and analytical transmission electron microscopy (TEM) were successfully employed to study carbon ingress and the chemical composition and microstructure of the reaction products.

A modeling framework has been used to evaluate these results that will benefit future studies in this area.

Publications and Other Results

R. G. Brese, J. R. Keiser and B. A. Pint, 2017, "Effect of Thermal Cycling on Compatibility in CO_2 for Concentrated Solar Power Applications," Oxidation of Metals, 87, 631-642. (also in *Proceedings of the 9th International Symposium on High Temperature Corrosion and Protection of Materials*, Les Embiez, France, May 2016, Paper#234). DOI: 10.1007/s11085-017-9762-0 https://www.osti.gov/biblio/1360028-effect-thermal-cycling-compatibility-co2-concentrated-solar-power-applications

B. A. Pint and R. G. Brese, 2017, "High-Temperature Materials Chapter 4 in Fundamentals and Applications of Supercritical Carbon Dioxide Based Power Cycles, K. Brun and P. Friedman, eds., Elsevier, London, pp.67-104. DOI: 10.1016/B978-0-08-100804-1.00004-9 https://www.osti.gov/biblio/1355882-high-temperature-materials

B. A. Pint, R. Brese and J. R. Keiser, 2017, "Effect of Pressure and Thermal Cycling on Compatibility in CO_2 for Concentrated Solar Power Applications," ASME Paper #GT2017-65066, for the International Gas Turbine & Aeroengine Congress & Exhibition, Charlotte, NC, June 26-30, 2017. https://www.osti.gov/servlets/purl/1376366

B. A. Pint, K. A. Unocic, R. G. Brese and J. R. Keiser, 2018, "Characterization of Chromia Scales Formed in Supercritical Carbon Dioxide," Materials at High Temperature 35, 39-49. DOI: 10.1080/09603409.2017.1389371 https://www.osti.gov/biblio/1424457-characterization-chromia-scales-formed-supercritical-carbon-dioxide

B. A. Pint and K. A. Unocic, 2018, "The Effect of CO_2 Pressure on Chromia Scale Microstructure at 750°C," JOM 70, 1511-1519. DOI: 10.1007/s11837-018-2963-4 https://www.osti.gov/biblio/1471923-effect-co2-pressure-chromia-scale-microstructure

B. A. Pint and J. R. Keiser, 2018, "The Effect of Impurities on Oxidation in Supercritical CO_2 at 750°C," in Proceedings of the 6th International Symposium on Supercritical CO_2 Power Cycles, Pittsburgh, PA, Paper #8.
http://sco2symposium.com/www2/sco2/papers2018/materials/008_Paper.pdf

M. J. Lance, D. N. Leonard and B. A. Pint, 2018, "The Use of Glow Discharge Optical Emission Spectroscopy to Quantify Internal Carburization in Supercritical CO_2," in Proceedings of the 6th International Symposium on Supercritical CO_2 Power Cycles, Pittsburgh, PA, Paper #117.
http://sco2symposium.com/www2/sco2/papers2018/materials/117_Paper.pdf

B. A. Pint, 2018, "Performance of Wrought Superalloys in Extreme Environments," in E. Ott et al. (Eds.), *Proceedings of the 9th International Symposium on Superalloy 718 and Derivatives*, TMS, Warrendale, PA, pp.165-178. DOI: 10.1007/978-3-319-89480-5_9 https://www.osti.gov/biblio/1471929-performance-wrought-superalloys-extreme-environments

B. A. Pint and J. R. Keiser, 2019, "Effect of Pressure and Thermal Cycling on Long-Term Oxidation in Supercritical CO_2," NACE Paper C2019-12750, Houston, TX, presented at NACE Corrosion 2019, Nashville, TN, March 2019.
https://www.osti.gov/servlets/purl/1505321

B. A. Pint, J. Lehmusto, M. J. Lance and J. R. Keiser, 2019, "The Effect of Pressure and Impurities on Oxidation in Supercritical CO_2," Mater. Corr., in press. DOI: 10.1002/maco.201810652

Award: B. A. Pint, 2016, ORNL Distinguished Researcher (1 of 2 awards for ~4800 person staff)

Mass change and oxide thickness data from this project will be published and linked to the published version of this report on OSTI.

Path Forward

The results of this projects have been communicated to the sCO₂ industrial community through numerous publications, presentations, conference calls and surveys. Significant investment was made in the experimental equipment for this project and ORNL is available to continue this research. There was never any plan to commercialize the results of this project. All of the results are openly available.

The mechanical testing subtasks were very valuable showing little debit in creep rupture lifetime at 750°C for exposure times of 100-3,000 h. However, the initial creep-fatigue results did show a debit in lifetime for 740H. A lesson learned is that it is difficult to execute mechanical testing on a fixed time schedule because of the uncertainty in failure times. As these data are extremely useful, it would be appropriate to continue the work but award projects on a fixed budget but allow for a no-cost extension.

One of the consistent feedbacks received from the sCO$_2$ community was that while the project was useful and appreciated, it did not address the entire sCO$_2$ cycle temperature range and a wider range of materials. A particular concern is material costs and guidance in the use (i.e. temperature limitations, e.g. [Sarrade 2017, Oleksak 2018]) for less-expensive steels such as creep-strength enhanced ferritic-martensitic Grade 91 (Fe-9Cr-1Mo) and conventional austenitic steels like type 316H or 347H. It may be useful to bring mechanical property evaluations into these lower temperature (450°-650°C) experiments by exposing small tensile specimens so that the tensile or creep properties can be evaluated post-exposure. Recent exposures at 750°C showed a degradation in ductility for 304H and HR3C (25Cr-20Ni) stainless steels for up to 4,000 h [Pint 2019b], however, that temperature is beyond the capability of these stainless steels.

Future work should partner with the STEP (Supercritical Transformational Electricity Production) facility to evaluate the effects of flowing sCO$_2$ under prototypical conditions and determine if erosion is an issue.

Finally, efforts to develop new materials for sCO$_2$, including coatings, require feedback about the role of composition on sCO$_2$ compatibility that is not currently available in the literature. For example, it is not clear how the advanced austenitic steels with higher levels of Cr and Ni perform in sCO$_2$. Similarly, lower cost Ni-base alloys with higher levels of Fe (10-30%) have not been sufficiently evaluated. Coatings rich in Cr and/or Al need to be evaluated. However, if erosion is an issue in flowing sCO2, then the formation of a thin reaction product in laboratory experiments but is susceptible to erosion in rapidly flowing sCO$_2$ fluid in a commercial system may not be an appropriate solution. The developments in modeling may help accelerate the needed assessments but modeling of the multiple processes involved without any experimental data is beyond the capability of current modeling.

Acknowledgments

material for evaluation. The project benefited from suggestions with DOE SETO project monitors, L. Irwin and M. Bauer.

References

R. J. Allam, Palmer, M. R., Brown Jr., G. W., Fetvedt, J., Freed, D., Nomoto, H., Itoh, M., Okita, N., Jones Jr., C., 2013, "High efficiency and low cost of electricity generation from fossil fuels while eliminating atmospheric emissions, including carbon dioxide," Energy Procedia 37, 1135–1149.

M. P. Brady, B. A. Pint, Z. G. Lu, J. H. Zhu, C. E. Milliken, E. D. Kreidler, L. Miller, T. R. Armstrong and L. R. Walker, 2006, "Comparison of Oxidation Behavior and Electrical Properties of Doped NiO- and Cr$_2$O$_3$-Forming Alloys for Solid Oxide Fuel Cell Metallic Interconnects," Oxidation of Metals, 65, 237-61.

R. G. Brese, J. R. Keiser and B. A. Pint, 2017, "Effect of Thermal Cycling on Compatibility in CO$_2$ for Concentrated Solar Power Applications," Oxidation of Metals, 87, 631-642.

G. Cao, V. Firouzdor, K. Sridharan, M. Anderson, T. R. Allen, 2012, "Corrosion of austenitic alloys in high temperature supercritical carbon dioxide," Corros. Sci. 60, 246-255.

R. Chacartegui, J. M. Muñoz De Escalona, D. Sánchez, B. Monje, and T. Sánchez, "Alternative cycles based on carbon dioxide for central receiver solar power plants," *Applied Thermal Engineering.* **31,** 5 (2011).

A. Chyrkin, P. Huczkowski, V. Shemet, L. Singheiser and W. J. Quadakkers, 2011, "Sub-Scale Depletion and Enrichment Processes During High Temperature Oxidation of the Nickel Base Alloy 625 in the Temperature Range 900-1000°C," Oxidation of Metals 75, 143-166.

J. J. deBarbadillo, B. A. Baker and R. D. Gollihue, 2014, "Nickel-Base Superalloys for Advanced Power Systems – An Alloy Producer's Perspective," in Proceedings of the 4th International Symposium on Supercritical CO2 Power Cycles, Pittsburgh, PA, September 2014, Paper #3.

V. Dheeradhada, A. Thatte, M. Karadge and M Drobnjak, "Corrosion of Supercritical CO₂ Turbomachinery Components," in Proceedings of the EPRI International Conference on Corrosion in Power Plants, Oct. 2015, San Diego, CA.

V. Dostal, P. Hejzlar and M. J. Driscoll, "High-Performance Supercritical Carbon Dioxide Cycle for Next-Generation Nuclear Reactors," Nuclear Technology, 154 (3) (2006) 265-282.

R. Duan, A. Jalowicka, K. A. Unocic, B. A. Pint, P. Huczkowski, A. Chyrkin, D. Grüner, R. Pillai and W. J. Quadakkers, 2016, "Predicting Oxidation-Limited Lifetime of Thin Walled Components of NiCrW alloy 230," Oxid. Met. 87 (2017) 11–38.

M. W. Dunlevy, 2009, "An Exploration of the Effect of Temperature on Different Alloys in Supercritical Carbon Dioxide Environment," M.Sc. Thesis, MIT, Cambridge, MA.

P. J. Ennis and W. J. Quadakkers, 1985, "Corrosion and Creep of Nickel-Base Alloys in Steam Reforming Gas," in High Temperature Alloys, Their Exploitable Potential, eds. J. B. Marriott, M. Merz, J. Nihoul and J. Ward, Elsevier, London, pp.465-474.

H. E. Evans, 1995, "Stress Effects in High Temperature Oxidation of Metals," International Materials Review 40, 1-40.

E. G. Feher, 1968, "The Supercritical Thermodynamic Power Cycle," Energy Conversion, 8, 85-90.

V. Firouzdor, K. Sridharan, G. Cao, M. Anderson, T. R. Allen, 2013, "Corrosion of a stainless steel and nickel-based alloys in high temperature supercritical carbon dioxide environment," Corros. Sci. 69, 281-291.

C. T. Fujii and R. A. Meussner, 1967, "Carburization of Fe-Cr Alloys During Oxidation in Dry Carbon Dioxide," J. Electrochem. Soc., 114, 435-442.

T. Furukawa, Y. Inagaki, M. Aritomi, Journal of Power and Energy Systems, 4 (2010) 252–261.

T. Furukawa, Y. Inagaki, M. Aritomi, "Compatibility of FBR structural materials with supercritical carbon dioxide," Progress in Nuclear Energy 53 (2011) 1050–1055.

T. Gheno, D. Monceau, J. Zhang and D. J. Young, "Carburisation of Ferritic Fe-Cr Alloys by Low Carbon Activity Gases," Corros. Sci., 53 (2011) 2767-2777.

T. Gheno, D. Monceau and D. J. Young, "Kinetics of breakaway oxidation of Fe-Cr and Fe-Cr-Ni alloys in dry and wet carbon dioxide," Corr. Sci. 77 (2013) 246-256.

Y. Gong, D. J. Young, P. Kontis, Y. L. Chiu, H. Larsson, A. Shin, J. M. Pearson, M. P. Moody and R. C. Reed, "On the breakaway oxidation of Fe9Cr1Mo steel in high pressure CO₂," *Acta Materialia*, 130 (2017) 361-374.

L. F. He, Roman, P., Leng, B., Sridharan, K., Anderson, M. Allen, T. R., 2014, "Corrosion behavior of an alumina forming austenitic steel exposed to supercritical carbon dioxide," Corros. Sci. 82, 67–76.

A. Jalowicka, R. Duan, P. Huczkowski, A. Chyrkin, D. Grüner, B. A. Pint, K. A. Unocic and W. J. Quadakkers, "Effect of Specimen Thickness on Microstructural Changes

During Oxidation of the NiCrW Alloy 230 at 950–1050°C," JOM 67(11) (2015) 2573-2588.

S. C. Kung, J. P. Shingledecker, D. Thimsen, I. G. Wright, B. M. Tossey, and A. S. Sabau, "Oxidation/Corrosion in Materials for Supercritical CO$_2$ Power Cycles," in Proceedings of the 5th International Symposium on Supercritical CO$_2$ Power Cycles, San Antonio, TX, March 2016, Paper #9.

S. C. Kung, J. P. Shingledecker, I. G. Wright, A. S. Sabau, B. M. Tossey, and T. Lolla, 2018, "Corrosion of Heat Exchanger Alloys in Open-Fired sCO$_2$ Power Cycles," in Proceedings of the 6th International Symposium on Supercritical CO$_2$ Power Cycles, Pittsburgh, PA, March 2018, Paper #5.

M. J. Lance, D. N. Leonard and B. A. Pint, 2018, "The Use of Glow Discharge Optical Emission Spectroscopy to Quantify Internal Carburization in Supercritical CO$_2$," in Proceedings of the 6th International Symposium on Supercritical CO$_2$ Power Cycles, Pittsburgh, PA, Paper #117.

H. J. Lee, H. Kim and C. Jang, "Compatibility of Candidate Structural Materials in High-Temperature s-CO$_2$ Environment" in Proceedings of the 4th International Symposium on Supercritical CO$_2$ Power Cycles, Pittsburgh, PA, September 2014, Paper #32.

H. J. Lee, H. Kim, S. H. Kim and C. Jang, 2015, "Corrosion and carburization behavior of chromia-forming heat resistant alloys in a high-temperature supercritical-carbon dioxide environment," Corrosion Science 99, 227–239.

J. Mahaffey, D. Adam, M. Anderson and K. Sridharan, (2016) "Effect of Oxygen Impurity on Corrosion in Supercritical CO$_2$ Environments," in Proceedings of the 5th International Symposium on Supercritical CO$_2$ Power Cycles, San Antonio, TX, March 2016, Paper #114.

H. E. McCoy, 1965, "Type 304 Stainless Steel vs Flowing CO2 at Atmospheric Pressure and 1100-1800°F," Corros., 21, 84-94.

G. H. Meier, W. C. Coons and R. A. Perkins, 1982, "Corrosion of Iron-, Nickel- and Cobalt-Base Alloys in Atmospheres Containing Carbon and Oxygen," Oxidation of Metals 17 (1982) 235-262.

G. H. Meier, K. Jung, N. Mu, N. M. Yanar, F. S. Pettit, J. Pirón Abellán, T. Olszewski, L. Nieto Hierro, W. J. Quadakkers and G. R. Holcomb, 2010, "Effect of Alloy Composition and Exposure Conditions on the Selective Oxidation Behavior of Ferritic Fe–Cr and Fe–Cr–X Alloys," Oxid. Met. 74, 319–340.

T. D. Nguyen, J. Q. Zhang and D. J. Young, "Microstructures of chromia scales grown in CO$_2$," Mater. High Temp. 32 (2015) 16-21.

C. H. Oh, Lillo, T., Windes, W., Totemeier, T., Ward, B., Moore, R., Barner, R., 2006, "Development of A Supercritical Carbon Dioxide Brayton Cycle: Improving VHTR Efficiency and Testing Material Compatibility," Idaho National Laboratory Report INL/EXT-06-01271.

R. P. Oleksak, J. H. Tylczak, C. S. Carney, G. R. Holcomb and O. N. Dogan, "High-Temperature Oxidation of Commercial Alloys in Supercritical CO_2 and Related Power Cycle Environments," JOM 70 (2018) 1527-1534.

R. I. Olivares, Young, D. J., Marvig, P., Stein, W., 2015, "Alloys SS316 and Hastelloy-C276 in Supercritical CO_2 at High Temperature," Oxid. Met. 84, 585–606.

B. Pieraggi, 1987, "Calculations of Parabolic Reaction Rate Constants," Oxid. Met., 27 (1987) 177-185.

L. M. Pike, 2008, "Development of a Fabricable Gamma-Prime (γ') Strengthened Superalloy," in Superalloys 2008, R. C. Reed et al. eds. TMS, Warrendale, PA, 2008, p.191-200.

R. Pillai, H. Ackermann, H. Hattendorf and S. Richter, 2013 "Evolution of Carbides and Chromium Depletion Profiles During Oxidation of Alloy 602CA," Corrosion Science 75, 28-37.

R. Pillai, W. G. Sloof, A. Chyrkin, L. Singheiser and W. J. Quadakkers, 2015, "A New Computational Approach for Modeling the Microstructural Evolution and Residual Lifetime Assessment of MCrAlY Coatings," Mater. High Temp. 32, 57-67.

B. A. Pint, J. R. DiStefano and I. G. Wright, 2006, "Oxidation Resistance: One Barrier to Moving Beyond Ni-Base Superalloys," Materials Science and Engineering A, 415, 255-263.

B. A. Pint, 2011, "The Future of Alumina-Forming Alloys: Challenges and Applications for Power Generation," Material Science Forum 696, 57-62.

B. A. Pint, B. N. Anderson, W. J. Matthews, C. Waldhelm and W. Treece, 2013, "Evaluation of NiCrAl Foil for a Concentrated Solar Power Application," ASME Paper #GT2013-94939, presented at the International Gas Turbine & Aeroengine Congress & Exhibition, San Antonio, TX, June 3-7, 2013.

B. A. Pint and J. R. Keiser, 2014, "The Effect of Temperature on the sCO_2 Compatibility of Conventional Structural Alloys," in Proceedings of the 4th International Symposium on Supercritical CO_2 Power Cycles, Pittsburgh, PA, September 2014, Paper #61.

B. A. Pint and J. R. Keiser, 2015a, "Initial Assessment of Ni-Base Alloy Performance in 0.1 MPa and Supercritical CO_2," JOM 67(11), 2615-2620.

B. A. Pint, Thiesing, B. P., 2015b, "Effect of Environment on the Oxidation Behavior of Commercial and Model Ni-Base Alloys," NACE Paper C2015-5919, Houston, TX, presented at NACE Corrosion 2015, Dallas, TX.

B. A. Pint, R. G. Brese and J. R. Keiser, 2016a, "Supercritical CO_2 Compatibility of Structural Alloys at 400°-750°C," NACE Paper C2016-7747, Houston, TX, presented at NACE Corrosion 2016, Vancouver, Canada, March 2016.

B. A. Pint, R. G. Brese and J. R. Keiser, 2016b "The Effect of Temperature and Pressure on Supercritical CO_2 Compatibility of Conventional Structural Alloys," in Proceedings of the 5th International Symposium on Supercritical CO_2 Power Cycles, San Antonio, TX, March 2016, Paper #56.

B. A. Pint, R. G. Brese and J. R. Keiser, 2016c "The Effect of O$_2$ and H$_2$O on oxidation in CO$_2$ at 700°-800°C," in Proceedings of the 5th International Symposium on Supercritical CO$_2$ Power Cycles, San Antonio, TX, March 2016, Paper #57.

B. A. Pint, R. G. Brese and J. R. Keiser, 2016d, "The Effect of Impurities on Supercritical CO$_2$ Compatibility of Structural Alloys," in Proc. 8th Inter. Conf. on Advances in Materials Technology for Fossil Power Plants, ASM International, Materials Park, OH, pp.845-855.

B. A. Pint, R. G. Brese and J. R. Keiser, 2017a, "Effect of Pressure on Supercritical CO$_2$ Compatibility of Structural Alloys at 750°C," Mater. Corros. 68, 151-158.

B. A. Pint and R. G. Brese, 2017b, "High-Temperature Materials Chapter 4 in Fundamentals and Applications of Supercritical Carbon Dioxide Based Power Cycles, K. Brun and P. Friedman, eds., Elsevier, London, pp.67-104.

B. A. Pint, R. Brese and J. R. Keiser, 2017c, "Effect of Pressure and Thermal Cycling on Compatibility in CO$_2$ for Concentrated Solar Power Applications," ASME Paper #GT2017-65066, for the International Gas Turbine & Aeroengine Congress & Exhibition, Charlotte, NC, June 26-30, 2017.

B. A. Pint, K. A. Unocic, R. G. Brese and J. R. Keiser, 2018a, "Characterization of Chromia Scales Formed in Supercritical Carbon Dioxide," Materials at High Temperature 35, 39-49.

B. A. Pint and K. A. Unocic, 2018b, "The Effect of CO$_2$ Pressure on Chromia Scale Microstructure at 750°C," JOM 70, 1511-1519.

B. A. Pint, R. G. Brese and J. R. Keiser, 2018c, "The effect of impurities and pressure on oxidation in CO$_2$ at 700°-800°C," NACE Paper C2018-11199, Houston, TX, presented at NACE Corrosion 2018, Phoenix, AZ.

B. A. Pint and J. R. Keiser, 2018d, "The Effect of Impurities on Oxidation in Supercritical CO$_2$ at 750°C," in Proceedings of the 6th International Symposium on Supercritical CO$_2$ Power Cycles, Pittsburgh, PA, Paper #8.

B. A. Pint, 2018e, "Performance of Wrought Superalloys in Extreme Environments," in E. Ott et al. (Eds.), *Proceedings of the 9th International Symposium on Superalloy 718 and Derivatives*, TMS, Warrendale, PA, pp.165-178.

B. A. Pint and J. R. Keiser, 2019a, "Effect of Pressure and Thermal Cycling on Long-Term Oxidation in Supercritical CO$_2$," NACE Paper C2019-12750, Houston, TX, presented at NACE Corrosion 2019, Nashville, TN, March 2019.

B. A. Pint, J. Lehmusto, M. J. Lance and J. R. Keiser, 2019b, "The Effect of Pressure and Impurities on Oxidation in Supercritical CO$_2$," Mater. Corr. in press.

W. J. Quadakkers and K. Bongartz, 1994 "The Prediction of Breakaway Oxidation for Alumina Forming ODS Alloys using Oxidation Diagrams," Werkst. Korros., 45, 232-241.

F. Rouillard, F. Charton, G. Moine, 2011 "Corrosion Behavior of Different Metallic Materials in Supercritical Carbon Dioxide at 550°C and 250 bars," Corros. 67(9), 095001.

H. Saari, C. Parks, R. Petrusenko, B. Maybee and K. Zanganeh, "Corrosion Testing of High Temperature Materials in Supercritical Carbon Dioxide," in Proceedings of the 4th International Symposium on Supercritical CO2 Power Cycles, Pittsburgh, PA, September 2014, Paper #64.

S. Sarrade, D Férona, F. Rouillard, S. Perrin, R. Robin, J.-C. Ruiz, H.-A. Turc, 2017, "Overview on corrosion in supercritical fluids," J. of Supercritical Fluids 120, 335–344.

L. Tan, M. Anderson, D. Taylor, T. R. Allen, 2011, "Corrosion of austenitic and ferritic-martensitic steels exposed to supercritical carbon dioxide," Corros. Sci. 53, 3273-3280.

C. S. Tedmon, 1966, "The Effect of Oxide Volatilization on the Oxidation Kinetics of Cr and Fe-Cr Alloys," Journal of the Electrochemical Society 113, 766-768.

C. Wagner, 1952 "Theoretical Analysis of the Diffusion Processes Determining the Oxidation Rate of Alloys," J. Electrochem. Soc., 99, 369-380.

D. J. Young, Zhang, J., Geers C., Schütze, M., 2011, "Recent advances in understanding metal dusting: A review," Mater. Corros. 62, 7-28.

D. J. Young, T. D. Nguyen, P. Felfer, J. Zhang and J. M. Cairney, 2014, "Penetration of protective chromia scales by carbon," Scripta Materialia 77, 29–32.

X. R. Zhang, H. Yamaguchi, D. Uneno, K. Fujima, M. Enomoto, N. Sawada, "Analysis of a novel solar energy-powered Rankine cycle for combined power and heat generation using supercritical carbon dioxide," Renewable Energy, 31 (2006) 1839-1854.